

A BAYESIAN APPROACH TO INFERRING FUNCTIONAL CONNECTIVITY GIVEN POPULATION CALCIUM IMAGING

BY YURIY MISHCHENKO* JOSHUA T. VOGELSTEIN[†], AND LIAM PANINSKI*

Deducing the structure of neural circuits from neural activity is one of the central problems of modern neuroscience. Recent studies have examined this problem by observing neural activity of dozens of neurons using multi-electrode techniques. Here, we present a model-based optimal approach for inferring structure of neural micro-circuits containing hundreds of neurons observed with calcium imaging. While calcium imaging allows less intrusive observations of neural activity in much larger populations than multi-electrode techniques, it provides only indirect observations of neural spike trains, which often may have limited time resolution and signal quality. To infer the functional connectivity matrix of neural micro-circuits from such indirect data, we assume a coupled hidden-Markov model, where each neuron is a generalized linear model. The sufficient statistics of the cross-coupling terms, i.e. the functional connectivity matrix, are obtained using an embedded-chain-within-blockwise-Gibbs algorithm, which produces samples of joint spike trains of all observed neurons given the calcium traces. By introducing a factorized approximation for the likelihood of such joint spike trains, we are able to implement our algorithm in parallel on a high-performance cluster, without a significant degradation of inference results. Imposing biophysically realistic constraints on our model, such as a sparseness of the connectivity matrix, facilitates a great reduction in the amount of data required to obtain a good fit. Thus, using realistic simulations of spontaneous activity in populations of randomly connected neurons, we show that our method can successfully infer the connectivity patterns from ~ 10 minutes of calcium imaging data for neural populations up to 500 neurons large, in approximately 10 minutes of computational time, and is robust to certain model misspecifications.

1. Introduction. Since Ramon y Cajal discovered that the brain is a rich and dense *network* of neurons (Ramon y Cajal, 1904; Ramon y Cajal, 1923), neuroscientists have been intensely curious about the details of these networks, which are believed to be the biological substrate for memory, cognition, and perception. While we have learned a great deal in the last century about “macro-circuits” — the connectivity between coarsely-defined brain areas — relatively little is known about “micro-circuits,” i.e., the connectivity within populations of neurons at a fine-grained cellular level. One can imagine two complementary strategies for inferring micro-circuits: anatomical and functional. Anatomical approaches to inferring circuitry do not rely on observing neural activity. Several interesting anatomical strategies are being pursued by other groups, such as array tomography (Micheva and Smith, 2007), “brainbow” mice (Livet et al., 2007), and serial electron microscopy (Briggman and Denk, 2006). Our work, takes a functional approach: our aim is to infer micro-circuits by observing the activity of a population of neurons.

*Department of Statistics and Center for Theoretical Neuroscience, Columbia University

[†]Johns Hopkins University

AMS 2000 subject classifications: Primary 60K35, 60K35; secondary 60K35

Keywords and phrases: sample, L^AT_EX 2_ε

Experimental tools that enable approximately simultaneous observations of the activity of many (e.g., $O(10^3)$) neurons are now widely available. While arrays of extracellular electrodes have been exploited for this purpose, the arrays most often used *in vivo* are inadequate for inferring monosynaptic connectivity in very large populations of neurons, as the inter-electrode spacing is typically too large to record from neighboring neurons, and technologically possible number of electrodes in the arrays limits the number of neurons that can be simultaneously observed (Hatsopoulos et al., 1998; Harris et al., 2003; Stein et al., 2004; Santhanam et al., 2006; Luczak et al., 2007)¹. Alternately, calcium-sensitive fluorescent indicators allow us to observe the spiking activity of up to $O(10^4)$ neighboring neurons (Tsien, 1989). Importantly, neighboring neurons are more likely connected to one another than distant neurons (Abeles, 1991; Braitenberg and Schuz, 1998). Some organic dyes achieve sufficiently high signal-to-noise ratios (SNR) that individual action potentials (spikes) may be resolved (Yuste et al., 2006), and bulk-loading techniques enable experimentalists to simultaneously fill populations of neurons with such dyes (Stosiek et al., 2003). In addition, genetically encoded calcium indicators are under rapid development in a number of groups, and are approaching SNR levels of nearly single spike accuracy as well (Wallace et al., 2008). Microscopy technologies for collecting fluorescence signals are also rapidly developing. Cooled CCDs for wide-field imaging (either epifluorescence or confocal) now achieve a quantum efficiency of $\approx 90\%$ with frame rates up to 60 Hz or greater, depending on the width of the field of view (Djurisic et al., 2004). For *in vivo* work, 2-photon laser scanning microscopy can achieve similar frame rates, using either acoustic-optical deflectors to focus light at arbitrary locations in three-dimensional space (Reddy and Saggau, 2005; Iyer et al., 2006; Salome et al., 2006; Reddy et al., 2008), or resonant scanners (Nguyen et al., 2001). Together, these experimental tools can provide movies of calcium fluorescence transients for small populations of neurons (e.g., $O(10^2)$) with “reasonable” SNR, and at imaging frequencies of 30 Hz or greater, in both the *in vitro* and *in vivo* settings.

Given these experimental advances in functional neural imaging, our goal is to develop efficient computational and statistical methods to exploit this data for the analysis of neural connectivity (see Fig. 3 for a schematic overview). One major challenge here is that calcium transients due to action potentials provide indirect observation of the neural activity, and decay about an order of magnitude slower than the time course of the underlying neural activity (Yuste et al., 2006). Thus, to properly analyze the functional network connectivity, we must incorporate a method for effectively deconvolving the observed noisy fluorescence signal to obtain estimates of the underlying spiking rates (Yaksi and Friedrich, 2006; Greenberg et al., 2008; Vogelstein et al., 2009). To this end we introduce a coupled Markovian state-space model that relates the observed variables (fluorescence traces from the neurons in the microscope’s field of view) to the hidden variables (spike trains and intracellular calcium concentrations of these neurons), as governed by a set of biophysical parameters including the network connectivity matrix. Given this model, we derive a Monte Carlo Expectation Maximization algorithm for obtaining the maximum a posteriori estimates of the parameters of interest. Standard Monte Carlo sampling procedures (e.g., Gibbs sampling or sequential Monte Carlo) are inadequate in this setting, due to the high dimensionality and non-linear, non-Gaussian dynamics of the hidden variables in our model; we therefore develop a spe-

¹It is worth noting, however, that multielectrode arrays which have been recently developed for use in the retina are capable of much denser sampling (Segev et al., 2004; Litke et al., 2004; Petrusca et al., 2007; Pillow et al., 2008).

cialized blockwise-Gibbs approach to overcome these obstacles. This strategy enables us to accurately infer the functional connectivity matrix from large simulated neural populations, under realistic assumptions about the dynamics and observation parameters. We describe our approach below, along with several methods for improving its computational speed and statistical efficiency.

2. Methods.

2.1. Model. We begin by detailing a parametric generative model for the (unobserved) joint spike trains of all N observable neurons, along with the observed calcium fluorescence data. Each neuron is modeled as a generalized linear model (GLM). This class of models is known to capture the statistical firing properties of individual neurons fairly accurately (Brillinger, 1988; Chornoboy et al., 1988; Brillinger, 1992; Plesser and Gerstner, 2000; Pillow et al., 2008; Paninski et al., 2004; Paninski, 2004; Rigat et al., 2006; Truccolo et al., 2005; Nykamp, 2007; Kulkarni and Paninski, 2007; Vidne et al., 2009; Stevenson et al., 2009). We denote the i -th neuron’s activity at time t as $n_i(t)$: in continuous time, $n_i(t)$ could be modeled as an unmarked point process, but we will take a discrete-time approach here, with each $n_i(t)$ taken to be a binary random variable. We model the spiking probability of neuron i via an instantaneous nonlinear function, $f(\cdot)$, of the filtered and summed input to that neuron at that time, $J_i(t)$. This input is composed of: (i) some baseline value, b_i ; (ii) some external vector stimulus, $S^{ext}(t)$, that is linearly filtered by k_i ; and (iii) spike history terms, $h_{ij}(t)$, encoding the influence on neuron i from neuron j , weighted by w_{ij} :

$$(1) \quad n_i(t) \sim \text{Bernoulli}[f(J_i(t))], \quad J_i(t) = b_i + k_i \cdot S^{ext}(t) + \sum_{j=1}^N w_{ij} h_{ij}(t).$$

To ensure computational tractability of the parameters inference problem, we must impose some reasonable constraints on the instantaneous nonlinearity $f(\cdot)$ (which plays the role of the inverse of the link function in the standard GLM setting) and on the dynamics of the spike-history effects $h_{ij}(t)$. First, we restrict our attention to functions $f(\cdot)$ which ensure the concavity of the spiking loglikelihood in this model (Paninski, 2004; Escola and Paninski, 2008), as we will discuss at more length below. In this paper, we use

$$(2) \quad f(J) = P[n > 0 \mid n \sim \text{Pois}(e^J \Delta)] = 1 - \exp[-e^J \Delta]$$

(Fig. 1), where the inclusion of Δ , the time step size, ensures that the firing rate scales properly with respect to the time discretization; see (Escola and Paninski, 2008) for a proof that this $f(\cdot)$ satisfies the required concavity constraints. However, we should note that in our experience the results depend only weakly on the details of $f(\cdot)$ within the class of log-concave models (Li and Duan, 1989; Paninski, 2004).

Second, because the algorithms we develop below assume Markovian dynamics, we model the spike history terms as an autoregressive process:

$$(3) \quad h_{ij}(t) = (1 - \Delta/\tau_{ij}^h) h_{ij}(t - \Delta) + n_j(t) + \sigma_{ij}^h \sqrt{\Delta} \epsilon_{ij}^h(t),$$

where τ_{ij}^h is the decay time constant for spike history terms, σ_{ij}^h is a standard deviation parameter, $\sqrt{\Delta}$ ensures that the statistics of this Markov process have a proper Ornstein-Uhlenbeck limit as $\Delta \rightarrow 0$, and throughout this paper, ϵ denotes an independent standard

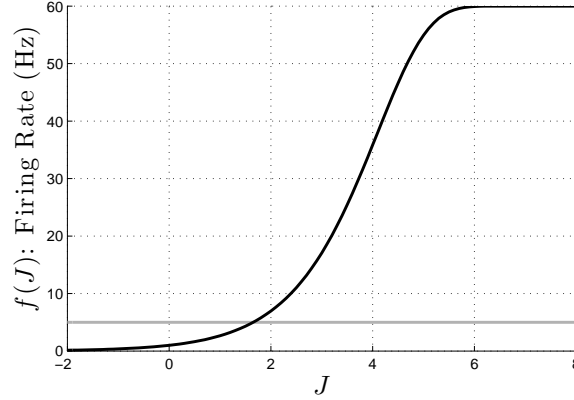


FIG 1. A plot of the firing rate nonlinearity $f(J)$ used in our simulations. Note that the firing rate saturates at $1/\Delta$, because of our Bernoulli assumption (i.e., the spike count per bin is at most one). Here $\Delta = (60 \text{ Hz})^{-1}$.

normal random variable. Note that this model generalizes (via a simple augmentation of the state variable $h_{ij}(t)$) to allow each neuron to have several spike history terms, each with a unique time constant, which when weighted and summed allow us to model a wide variety of possible post-synaptic effects, including bursting, facilitating, and depressing synapses; see (Vogelstein et al., 2009) for further details. We restrict our attention to the case of a single time constant τ_{ij}^h here, so the deterministic part of $h_{ij}(t)$ is a simple exponential function. Furthermore, we assume that τ_{ij}^h is the same for all neurons and all synapses, although in principle each synapse could be modeled with its unique τ_{ij}^h . We do that both for simplicity and also because we find that the detailed shape of the coupling terms $h_{ij}(t)$ had a limited effect on the inference of the connectivity matrix, as illustrated in Fig. 12 below. Thus, we treat τ_{ij}^h and σ_{ij}^h as known synaptic parameters which are the same for each neuron pair (i, j) ; therefore our unknown model spiking parameters are $\{\mathbf{w}_i, k_i, b_i\}_{i \leq N}$, with $\mathbf{w}_i = (w_{i1}, \dots, w_{iN})$.

The problem of estimating the connectivity parameters $\mathbf{w} = \{\mathbf{w}_i\}_{i \leq N}$ in this type of GLM, given a fully-observed ensemble of neural spike train $\{n_i(t)\}_{i \leq N}$, has recently received a great deal of attention; see the references above for a partial list. In the calcium fluorescent imaging setting, however, we do not directly observe spike trains; $\{n_i(t)\}_{i \leq N}$ must be considered a hidden variable here. Instead, each spike in a given neuron leads to a rapid increase in the intracellular calcium concentration, which then decays slowly due to various cellular buffering and extrusion mechanisms. We in turn make only noisy, indirect, and subsampled observations of this intracellular calcium concentration, via fluorescent imaging techniques (Yuste et al., 2006). To perform statistical inference in this setting, (Vogelstein et al., 2009) proposed a simple conditional first-order hidden Markov model (HMM) for the intracellular calcium concentration $C_i(t)$ in cell i at time t , along with the observed fluorescence, $F_i(t)$:

$$(4) \quad C_i(t) = C_i(t - \Delta) + (C_i^b - C_i(t - \Delta))\Delta/\tau_i^c + A_i n_i(t) + \sigma_i^c \sqrt{\Delta} \epsilon_i^c(t),$$

$$(5) \quad F_i(t) = \alpha_i S(C_i(t)) + \beta_i + \sqrt{\gamma_i S(C_i(t)) + \sigma_i^F} \epsilon_i^F(t).$$

This model can be interpreted as a simple driven autoregressive process: under nonspiking conditions, $C_i(t)$ fluctuates around the baseline level of C_i^b , driven by normally-distributed noise $\epsilon_i^c(t)$ with standard deviation $\sigma_i^c \sqrt{\Delta}$. Whenever the neuron fires a spike, $n_i(t) = 1$, the calcium variable $C_i(t)$ jumps by a fixed amount A_i , and subsequently decays with time

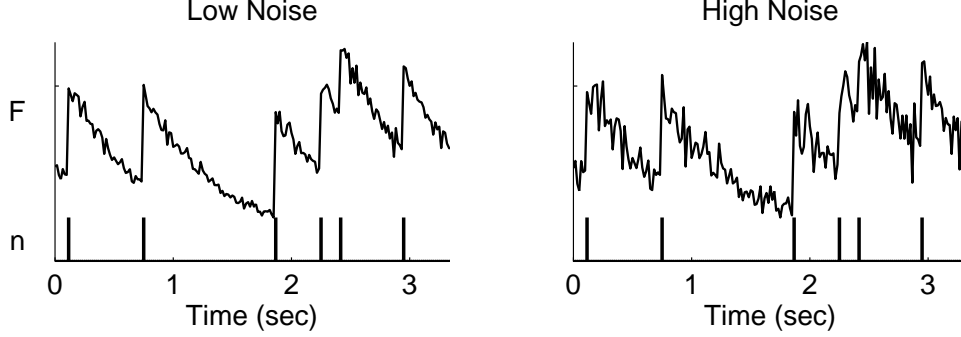


FIG 2. Both a low and high noise simulation showing typical relationships between spike trains and observations. Note that both panels have the same underlying spike train. Simulation parameters: $k_i = 0.7$, $C_i^b = 1 \mu M$, $\tau_i^c = 500 \text{ msec}$, $A_i = 50 \mu M$, $\sigma_i^c = 0.1 \mu M$, $\alpha = 2$, $\beta = 0$, $\gamma = 0.004, 0.016$ (left panel, right panel, respectively), $\sigma_i^F = 0$. $\Delta = 1/60 \text{ Hz}$.

constant τ_i^c . The fluorescence signal $F_i(t)$ corresponds to the count of photons collected at the detector per neuron per imaging frame. This photon count may be modeled with normal statistics, with the mean given by a scaled and shifted Hill function $S(C) = C/(C + K_d)$ (Yasuda et al., 2004) and the variance proportional to the mean (which follows from assuming the Poisson statistics of the photon counts are well approximated with Normal distribution; see (Vogelstein et al., 2009) for further discussion. Because the parameter K_d effectively acts as a simple scale factor, and is a property of the fluorescent indicator, we assume throughout this work that it is known. Figure 2 shows a couple examples depicting the relationship between spike trains and observations.

To summarize, Eqs. (1) – (5) define a coupled HMM: the underlying spike trains $\{n_i(t)\}_{i \leq N}$ and spike history terms $\{h_{ij}(t)\}_{i,j \leq N}$ evolve in a Markovian manner given the stimulus $S^{ext}(t)$. These spike trains in turn drive the intracellular calcium concentrations $\{C_i(t)\}_{i \leq N}$, which are themselves Markovian, but evolving at a slower timescale τ_i^c . Finally, we observe only the fluorescence signals $\{F_i(t)\}_{i \leq N}$, which are related in a simple Markovian fashion to the calcium variables $\{C_i(t)\}_{i \leq N}$.

2.2. Goal and general strategy. Our primary goal is to estimate the connectivity matrix, \mathbf{w} , given the observed set of calcium fluorescence signals $\mathbf{F} = \{\mathbf{F}(t)\}_{t \leq T}$ and $\mathbf{F}(t) = \{F_i(t)\}_{i \leq N}$. We must also deal with a number of nuisance parameters, $\tilde{\theta}_i$: the intrinsic dynamics parameters $\{k_i, b_i, w_{ii}\}_{i \leq N}$, the calcium parameters $\{C_i^b, \tau_i^c, A_i, \sigma_i^c\}_{i \leq N}$, and the observation parameters $\{\alpha_i, \beta_i, \gamma_i, \sigma_i^F\}_{i \leq N}$. We addressed the problem of estimating these latter parameters in earlier work (Vogelstein et al., 2009); thus our focus here will be on the connectivity matrix \mathbf{w} . A Bayesian approach is natural here, since we have a good deal of prior information about neural connectivity; see (Rigat et al., 2006) for a related discussion. However, a fully-Bayesian approach, in which we numerically integrate over the very high-dimensional parameters' space $\theta = \{\theta_i\}_{i \leq N}$, where $\theta_i = \{\mathbf{w}_i, k_i, b_i, C_i^b, \tau_i^c, A_i, \sigma_i^c, \alpha_i, \beta_i, \gamma_i, \sigma_i^F\}$, is not particularly attractive from a computational point of view². Thus, our compromise is to compute *maximum a posteriori* (MAP) estimates for the parameters via an expectation-maximization (EM) algorithm in which the sufficient statistics are computed by a hybrid blockwise Gibbs sampler and

²The nuisance parameters for neuron i are all its parameters, minus the cross-coupling terms, i.e. $\tilde{\theta}_i = \theta_i \setminus \{w_{ij}\}_{i \neq j}$.

sequential Monte Carlo (SMC) method. More specifically, we iterate the steps:

E step: Evaluate $Q(\theta, \theta^{(l)}) = E_{P[\mathbf{X}|\mathbf{F}; \theta^{(l)}]} \ln P[\mathbf{F}, \mathbf{X}|\theta] = \int P[\mathbf{X}|\mathbf{F}; \theta^{(l)}] \ln P[\mathbf{F}, \mathbf{X}|\theta] d\mathbf{X}$

M step: Solve $\theta^{(l+1)} = \underset{\theta}{\operatorname{argmax}} \left\{ Q(\theta, \theta^{(l)}) + \ln P(\theta) \right\},$

where \mathbf{X} denotes the set of all hidden variables $\{C_i(t), n_i(t), h_{ij}(t)\}_{i,j \leq N, t \leq T}$ and $P(\theta)$ denotes a (possibly improper) prior on the parameter space θ . According to standard EM theory (Dempster et al., 1977; McLachlan and Krishnan, 1996), each iteration of these two steps is guaranteed to increase the log-posterior $\ln P(\theta^{(l)}|\mathbf{F})$, and will therefore lead to at least a locally maximum a posteriori estimator.

Now, our major challenge is to evaluate the auxiliary function $Q(\theta, \theta^{(l)})$ in the E-step. Our model is a coupled HMM, as discussed in the previous section; therefore, as usual in the HMM setting (Rabiner, 1989), Q may be broken up into a sum of simpler terms:

$$\begin{aligned}
 Q(\theta, \theta^{(l)}) &= \sum_{it} P[C_i(t)|F_i; \tilde{\theta}_i] \times \ln P[F_i(t)|C_i(t); \alpha_i, \beta_i, \gamma_i, \sigma_i^F] \\
 &+ \sum_{it} P[C_i(t), C_i(t - \Delta), n_i(t)|F_i; \tilde{\theta}_i] \times \ln P[C_i(t)|C_i(t - \Delta), n_i(t); C_i^b, \tau_i^c, A_i, \sigma_i^c] \\
 (6) \quad &+ \sum_{it} P[n_i(t), \mathbf{h}_i(t)|\mathbf{F}; \theta_i] \times \ln P[n_i(t)|\mathbf{h}_i(t); b_i, k_i, \mathbf{w}_i, S^{ext}(t)]
 \end{aligned}$$

where $\mathbf{h}_i(t) = \{h_{ij}(t)\}_{j \leq N}$. Note that each of the three sums here corresponds to a different component of the model described in Eqs. (1) – (5): the first sum involves the fluorescent observation parameters, the second the calcium dynamics, and the third the spiking dynamics (note the absence of a term for the spike history terms, as their parameters are assumed known a priori).

Thus we need only compute low-dimensional marginals of the full posterior distribution $P[\mathbf{X}|\mathbf{F}; \theta]$; specifically, we need pairwise marginals, of the form $P[C_i(t), C_i(t - \Delta)|F_i; \tilde{\theta}_i]$, and marginals $P[C_i(t)|F_i; \tilde{\theta}_i]$ and $P[n_i(t), \mathbf{h}_i(t)|\mathbf{F}; \theta_i]$. Details for calculating $P[C_i(t), C_i(t - \Delta)|F_i; \tilde{\theta}_i]$ and $P[C_i(t)|F_i; \tilde{\theta}_i]$ are found in (Vogelstein et al., 2009). Calculation of the joint marginal for high dimensional hidden variable \mathbf{h}_i necessitates the development of specialized blockwise Gibbs-SMC sampling method, as we describe in the subsequent sections 2.3 and 2.4. Once we have obtained these marginals, the M-step breaks up into a number of independent optimizations that may be computed in parallel and which are therefore relatively straightforward (Section 2.5); see section 2.6 for a pseudocode summary along with some specific implementation details.

2.3. Initialization of nuisance parameters via sequential Monte Carlo methods. We begin by constructing relatively cheap, approximate preliminary estimators for the nuisance parameters, $\tilde{\theta}_i$. The idea is to initialize our estimator by assuming that each neuron is observed independently. Thus we want to compute $P[C_i(t), C_i(t - \Delta)|F_i; \tilde{\theta}_i]$ and $P[C_i(t)|F_i; \tilde{\theta}_i]$, and solve the M-step for each $\tilde{\theta}_i$, with the connectivity matrix parameters held fixed. This single-neuron case is much simpler, and has been discussed at length in (Vogelstein et al., 2009); therefore, we only provide a brief overview here. The standard forward and backward

recursions provide these posteriors (Shumway and Stoffer, 2006):

(7)

$$P[X_i(t)|F_i(0:t)] \propto P[F_i(t)|X_i(t)] \int P[X_i(t)|X_i(t-\Delta)]P[X_i(t-\Delta)|F_i(0:t-\Delta)]dX_i(t-\Delta),$$

(8)

$$P[X_i(t), X_i(t-\Delta)|F_i] = P[X_i(t)|F_i] \frac{P[X_i(t)|X_i(t-\Delta)]P[X_i(t-\Delta)|F_i(0:t-\Delta)]}{\int P[X_i(t)|X_i(t-\Delta)]P[X_i(t-\Delta)|F_i(0:t-\Delta)]dX_i(t-\Delta)},$$

where $F_i(s:t)$ denotes the time series F_i from time points s to t , and we have dropped the conditioning on the parameters for brevity's sake. Eq. (7) describes the forward (filter) pass of the recursion, and Eq. (8) describes the backward (smoother) pass, providing both $P[X_i(t), X_i(t-\Delta)|F_i]$ and $P[X_i(t)|F_i]$ (obtained by marginalizing by $X_i(t-\Delta)$).

Because these integrals cannot be analytically evaluated for our model, we approximate them using a SMC (“marginal particle filtering”) method (Doucet et al., 2000; Doucet et al., 2001; Godsill et al., 2004); see (Vogelstein et al., 2009) for details on the proposal density and resampling methods used here. The output of this SMC method comprises an array of particle positions $\{X_i^{(m)}(t)\}_{m=1}^M$, where m indexes the particle number, and a discrete approximation to the marginals $P[X_i(t), X_i(t-\Delta)|F_i]$,

$$(9) \quad P[X_i(t), X_i(t-\Delta)|F_i] \approx$$

$$\approx \sum_{m,m'} r_i^{(m,m')}(t, t-\Delta) \delta[X_i(t) - X_i^{(m)}(t)] \delta[X_i(t-\Delta) - X_i^{(m')}(t-\Delta)],$$

where $r_i^{(m,m')}(t, t-\Delta)$ denotes the weight attached to the pair of particles with positions $(X_i^{(m)}(t), X_i^{(m')}(t-\Delta))$, and $\delta(\cdot)$ denotes a Dirac mass.

As discussed above, the sufficient statistics for estimating the nuisance parameters for each neuron, $\tilde{\theta}_i$, are exactly these marginal posteriors. As discussed following Eq. (6), the M-step decouples into three independent subproblems. The first term depends on only $\{\alpha_i, \beta_i, \gamma_i, \sigma_i\}$; since $P[F_i(t)|S(C_i(t)); \tilde{\theta}_i]$ is quadratic (by our Gaussian assumption on the fluorescent observation noise), we can estimate these parameters by solving a weighted regression problem (specifically, we use a coordinate-optimization approach: we solve a quadratic problem for $\{\alpha_i, \beta_i\}$ while holding $\{\gamma_i, \sigma_i\}$ fixed, then estimate $\{\gamma_i, \sigma_i\}$ by the usual residual error formulas while holding $\{\alpha_i, \beta_i\}$ fixed). Similarly, the second term requires us to optimize over $\{\tau_i^c, A_i, C_i^b\}$, and then we use the residuals to estimate σ_i^c . Note that all the parameters mentioned so far are constrained to be non-negative, but may be solved efficiently using standard quadratic program solvers if we use the simple reparameterization $\tau_i^c \rightarrow 1 - \Delta/\tau_i^c$. Finally, the last term, assuming neurons are independent, may be expanded:

$$(10) \quad E[\ln P[n_i(t), \mathbf{h}_i(t)|\mathbf{F}; \theta_i]] =$$

$$= P[n_i(t), \mathbf{h}_i(t)|\mathbf{F}] \ln f[J_i(t)] + (1 - P[n_i(t), \mathbf{h}_i(t)|\mathbf{F}]) \ln[1 - f(J_i(t))];$$

since $J_i(t)$ is a linear function of $\{b_i, k_i, \mathbf{w}_i\}$, and the right-hand side of Eq. (10) is concave in $J_i(t)$, we see that the third term in Eq. (6) is a sum of terms which are concave in $\{b_i, k_i, \mathbf{w}_i\}$ — and therefore also concave in the linear subspace $\{b_i, k_i, w_{ii}\}$ with $\{w_{ij}\}_{i \neq j}$ held fixed — and may thus be maximized efficiently using any convex optimization method, e.g. Newton-Raphson or conjugate gradient ascent.

Our procedure therefore is to initialize the parameters for each neuron using some default values that we have found to be practically effective in analyzing real data, and then recursively (i) estimate the marginal posteriors via Eq. (9) (E step), and (ii) maximize the nuisance parameters $\tilde{\theta}_i$ (M step), using the above described approach. We iterate these two steps until the change in θ_i does not exceed some minimum threshold (or we reach an upper bound on iterations). We then use the marginal posteriors from the last iteration to seed the blockwise Gibbs sampling procedure described below. With that, we approximate $P[n_i, \mathbf{h}_i | \mathbf{F}; \theta_i]$.

2.4. Estimating joint posteriors over weakly coupled neurons. Now we turn to the key problem: constructing an estimate of the joint marginals $\{P[n_i(t), \mathbf{h}_i(t) | \mathbf{F}; \theta]\}_{i \leq N}$, which are the sufficient statistics for estimating the connectivity matrix \mathbf{w} (recall Eq. (6)). The SMC method described in the preceding section only provide the marginals over each neuron; this method may in principle be extended to obtain the desired full posterior $P[\mathbf{X}(t), \mathbf{X}(t-\Delta) | \mathbf{F}; \theta]$, but the SMC is fundamentally a sequential importance sampling method, and therefore scales poorly as the dimensionality of the hidden state $\mathbf{X}(t)$ increases (Bickel et al., 2008). Thus we need a different approach.

One very simple idea is to use a Gibbs sampler: sample sequentially from

$$(11) \quad X_i(t) \sim P[X_i(t) | \mathbf{X}_{\setminus i}, X_i(0), \dots, X_i(t-\Delta), X_i(t+\Delta), \dots, X_i(T), \mathbf{F}; \theta],$$

looping over all cells i and all time bins t . Unfortunately, this approach is likely to mix poorly, due to the strong temporal dependence between $X_i(t)$ and $X_i(t+\Delta)$. Instead, we propose a blockwise Gibbs strategy, sampling one spike train as a block:

$$(12) \quad X_i \sim P[X_i | \mathbf{X}_{\setminus i}, \mathbf{F}; \theta].$$

If we can draw these blockwise samples $X_i = X_i(s:t)$ efficiently for a large subset of $t-s$ adjacent time-bins simultaneously, then we would expect the resulting Markov chain to mix much more quickly than the single-element Gibbs chain. This follows due to the weak dependence between X_i and X_j when $i \neq j$, and that Gibbs is most efficient for weakly-dependent variables (Robert and Casella, 2005).

So, how can we efficiently sample from $P[X_i | \mathbf{X}_{\setminus i}, \mathbf{F}; \theta]$? One attractive approach is to try to re-purpose the SMC method described above, which is quite effective for drawing approximate samples from $P[X_i | \mathbf{X}_{\setminus i}, F_i; \theta]$ for one neuron i at a time. Recall that sampling from an HMM is in principle easy by the “propagate forward, sample backward” method: we first compute the forward probabilities $P[X_i(t) | \mathbf{X}_{\setminus i}(0:t), F_i(0:t); \theta]$ recursively for timesteps 0 up to T , then sample backwards from $P[X_i(t) | \mathbf{X}_{\setminus i}(0:T), F_i(0:T), X_i(t-\Delta); \theta]$. This approach is powerful because each sample requires just linear time to compute (i.e., $O(T/\Delta)$ time, where T/Δ is the number of desired time steps). Unfortunately, in this case we can only compute the forward probabilities approximately (with the SMC forward recursion approximation to Eq. (7)), and so therefore this attractive forward-backward approach only provides approximate samples from $P[X_i | \mathbf{X}_{\setminus i}, \mathbf{F}; \theta]$, not the exact samples required for the validity of the Gibbs method.

Of course, in principle we should be able to use the Metropolis-Hastings (M-H) algorithm to correct these approximate samples. The problem is that the M-H acceptance ratio in this setting involves a high-dimensional integral over the set of paths that the particle filter might possibly trace out, and is therefore difficult to compute directly. (Andrieu et al., 2007) discuss this problem at more length, along with some proposed solutions. A slightly simpler approach was introduced by (Neal et al., 2003). Their idea is to exploit the $O(T/\Delta)$ forward-backward sampling method by embedding a discrete Markov chain within the continuous state

space \mathcal{X}_t ; the state space of this discrete embedded chain is sampled randomly according to some distribution ρ_t with support on \mathcal{X}_t . It turns out that an appropriate acceptance probability (defined in terms of the original state space model transition and observation probabilities, along with the auxiliary sampling distributions ρ_t) may be computed quite tractably, guaranteeing that the samples produced by this algorithm form a Markov chain with the desired equilibrium density. See (Neal et al., 2003) for details.

We can apply this embedded-chain method quite directly here to sample from $P[X_i|\mathbf{X}_{\setminus i}, \mathbf{F}; \theta]$. The one remaining question is how to choose the auxiliary densities ρ_t . We would like to choose these densities to be close to the desired marginal densities $P[X_i(t)|\mathbf{X}_{\setminus i}, \mathbf{F}; \theta]$, and conveniently, we have already computed a good (discrete) approximation to these densities, using the SMC methods described in the last section. The algorithm described in (Neal et al., 2003) requires that ρ_t be continuous densities, so we simply convolve our discrete SMC-based approximation (specifically, the $X_i(t)$ -marginal of Eq. (9)) with an appropriate normal density to arrive at a very tractable mixture-of-Gaussians representation for ρ_t with required properties.

Thus, to summarize, our procedure for approximating the desired joint state distributions $P[n_i(t), \mathbf{h}_i(t)|\mathbf{F}; \theta_i]$ has a Metropolis-within-blockwise-Gibbs flavor, where the internal Metropolis step is replaced by the $O(T/\Delta)$ embedded-chain method introduced by (Neal et al., 2003), and the auxiliary densities ρ_t necessary for implementing the embedded-chain sampler are obtained using the SMC methods from (Vogelstein et al., 2009).

2.4.1. A factorized approximation of the joint posteriors. If the SNR in the calcium imaging is sufficiently high, then by definition the observed fluorescence data F_i will provide enough information to determine the underlying hidden variables X_i . Thus, in this case the joint posterior approximately factorizes into a product of marginals for each neuron i :

$$(13) \quad P[\mathbf{X}(t)|\mathbf{F}; \theta] \approx \prod_{i \leq N} P[X_i(t)|F_i; \tilde{\theta}_i].$$

We can take advantage of this because we have already estimated all the above marginals using the SMC method in Section 2.3. This factorized approximation entails a very significant gain in efficiency for two reasons: first, it obviates the need to generate joint samples via the expensive blockwise-Gibbs approach described above; and second, because we can very easily parallelize the SMC step, inferring the marginals $P[X_i(t)|F_i; \tilde{\theta}_i]$ and estimating the parameters θ_i for each neuron on a separate processor. We will discuss the empirical accuracy of this approximation the Results section.

2.5. Estimating the functional connectivity matrix. Computing the M-step for the connectivity matrix, \mathbf{w} , is an optimization problem with on the order of N^2 variables. The auxiliary function Eq. (6) is concave in \mathbf{w} , and decomposes into N separable terms that may be optimized independently using standard ascent methods. To improve our estimates, we will incorporate two sources of strong *a priori* information via our prior $P(\mathbf{w})$: first, previous anatomical studies have established that connectivity in many neuroanatomical substrates is “sparse,” i.e., most neurons form synapses with only a fraction of their neighbors (Buhl et al., 1994; Thompson et al., 1988; Reyes et al., 1998; Feldmeyer et al., 1999; Gupta et al., 2000; Feldmeyer and Sakmann, 2000; Petersen and Sakmann, 2000; Binzegger et al., 2004; Song et al., 2005; Mishchenko et al., 2009), implying that many elements of the connectivity matrix \mathbf{w} are zero; see also (Paninski, 2004; Rigat et al., 2006; Pillow et al., 2008; Stevenson

et al., 2008) for further discussion. Second, “Dale’s law” states that each of a neuron’s postsynaptic connections in adult cortex (and many other brain areas) must all be of the same sign (either excitatory or inhibitory). Both of these priors are easy to incorporate in the M-step optimization, as we discuss below.

2.5.1. Imposing a sparse prior on the functional connectivity. It is well-known that imposing sparseness via an $L1$ -regularizer can dramatically reduce the amount of data necessary to accurately reconstruct sparse high-dimensional parameters (Tibshirani, 1996; Tipping, 2001; Donoho and Elad, 2003; Ng, 2004; Candes and Romberg, 2005; Mishchenko, 2009). We incorporate a prior of the form $\ln p(\mathbf{w}) = \text{const.} - \lambda \sum_{i,j} |w_{ij}|$, and additionally enforce the constraints $|w_{ij}| < M$, for a suitable constant M (since both excitatory and inhibitory cortical connections are known to be bounded in size). Since the penalty $\ln p(\mathbf{w})$ is concave, and the constraints $|w_{ij}| < M$ are convex, we may solve the resulting optimization problem in the M-step using standard convex optimization methods (Boyd and Vandenberghe, 2004). In addition, the problem retains its separable structure: the full optimization may be broken up into N smaller problems that may be solved independently.

2.5.2. Imposing Dale’s law on the functional connectivity. Enforcing Dale’s law requires us to solve a non-convex, non-separable problem: we need to optimize the concave function $Q(\theta, \theta^{(l)}) + \ln P(\theta)$ under the non-convex, non-separable constraint that all of the elements in any column of the matrix \mathbf{w} are of a definite sign (either nonpositive or nonnegative). It is difficult to solve this nonconvex problem exactly, but we have found that simple greedy methods are quite efficient in finding good approximate solutions.

We begin with our original sparse solution, obtained as discussed in the previous subsection without enforcing Dale’s law. Then we assign each neuron as either excitatory or inhibitory, based on the weights we have inferred in the previous step: i.e., neurons i whose inferred postsynaptic connections w_{ij} are largely positive are tentatively labeled excitatory, and neurons with largely inhibitory inferred postsynaptic connections are labeled inhibitory. Neurons which are highly ambiguous may be unassigned in the early iterations, to avoid making mistakes from which it might be difficult to recover. Given the assignments a_i ($a_i = 1$ for putative excitatory cells, -1 for inhibitory, and 0 for neurons which have not yet been assigned) we solve the convex, separable problem

$$(14) \quad \underset{a_i w_{ij} \geq 0, |w_{ij}| < M \quad \forall i,j}{\operatorname{argmax}} \quad Q(\theta, \theta^{(l)}) - \lambda \sum_{ij} |w_{ij}|$$

which may be handled using the standard convex methods discussed above. Given the new estimated connectivities \mathbf{w} , we can re-assign the labels a_i , or even flip some randomly to check for local optima. We have found this simple approach to be effective in practice.

2.6. Specific implementation notes. Pseudocode summarizing our approach is given in Algorithm 1. As discussed in Section 2.3, the nuisance parameters $\tilde{\theta}_i$ may be initialized effectively using the methods described in (Vogelstein et al., 2009); then the full parameter θ is estimated via EM, where we use the embedded-chain-within-blockwise-Gibbs approach discussed in Section 2.4 (or the cheaper factorized approximation described in Section 2.4.1) to obtain the sufficient statistics in the E step and the separable convex optimization methods discussed in Section 2.5 for the M step.

As emphasized above, the parallel nature of these EM steps is essential for making these computations tractable. We performed the bulk of our analysis on a 100-node cluster of

Algorithm 1 Pseudocode for estimating functional connectivity from calcium imaging data using EM; η_1 and η_2 are user-defined convergence tolerance parameters.

```

while  $|\mathbf{w}^{(t)} - \mathbf{w}^{(t-1)}| > \eta_1$  do
  for all  $i = 1 \dots N$  do
    while  $|\hat{\theta}_i^{(t)} - \hat{\theta}_i^{(t-1)}| > \eta_2$  do
      Approximate  $P[X_i(t)|F_i; \tilde{\theta}_i]$  using SMC (Section 2.3)
      Perform the M-step for the nuisance parameters  $\tilde{\theta}_i$  (Section 2.3)
    end while
  end for
  for all  $i = 1 \dots N$  do
    Approximate  $P[n_i(t), \mathbf{h}_i(t)|\mathbf{F}; \theta_i]$  using either the blockwise Gibbs
    method or the factorized approximation (Section 2.4)
  end for
  for all  $i = 1 \dots N$  do
    Perform the M-step on  $\theta_i$  using separable convex optimization methods (Section 2.5)
  end for
end while

```

Intel Xeon L5430 based computers (2.66 GHz). For 10 minutes of simulated fluorescence data, imaged at 30 Hz, calculations using the factorized approximation typically took 10-20 minutes per neuron (divided by the number of available processing nodes on the cluster), with time split approximately equally between (i) estimating the nuisance parameters $\tilde{\theta}_i$, (ii) approximating the posteriors using the independent SMC method, and (iii) estimating the functional connectivity matrix, \mathbf{w} . The hybrid embedded-chain-within-blockwise-Gibbs sampler was substantially slower, up to an hour per neuron per Gibbs pass, with the Gibbs sampler dominating the computation time, because we thinned the chain by a factor of five (since we found empirically that the autocorrelation of the Gibbs chain had a scale of about five time steps).

2.7. Simulating a neural population. To test the described method for inferring functional connectivity from calcium imaging data, we simulated networks (according to our model, Eqs. (1) – (5)) of spontaneously firing randomly connected neurons. Although simulations ran at 1 msec time discretization, imaging rate was assumed to be much slower: 5–200 Hz. Simulations lasted anywhere between 5 minutes and 1 hours (of simulated time).

Model parameters were chosen based on experimental data available in the literature for cortical neural networks (Braitenberg and Schuz, 1998; Gomez-Urquijo et al., 2000; Lefort et al., 2009; Sayer et al., 1990). More specifically, the network contained 80% of excitatory and 20% inhibitory neurons (Braitenberg and Schuz, 1998; Gomez-Urquijo et al., 2000), each respecting Dale’s law. Neurons were randomly connected to each other with probability 0.1 (Braitenberg and Schuz, 1998; Lefort et al., 2009). Synaptic weights for excitatory connections, as defined by EPSP peak amplitude, were randomly drawn from exponential distribution with the mean of $0.5\mu V$ (Lefort et al., 2009; Sayer et al., 1990). Inhibitory connections were also drawn from exponential distribution; their strengths chosen so as to balance excitatory and inhibitory currents in the network, and achieve an average firing rate of ≈ 5 Hz (Abeles, 1991). Practically, this meant that the mean strength of inhibitory connections was about 10 times larger than that of the excitatory connections. PSP shapes were modeled as an alpha function (Koch, 1999), by differencing two exponentials, corresponding to a sharp rise and relatively slow decay (Sayer et al., 1990). We neglected conduction delays, given that the time delay below ~ 1 msec expected in local cortical circuit was smaller than the time step of our

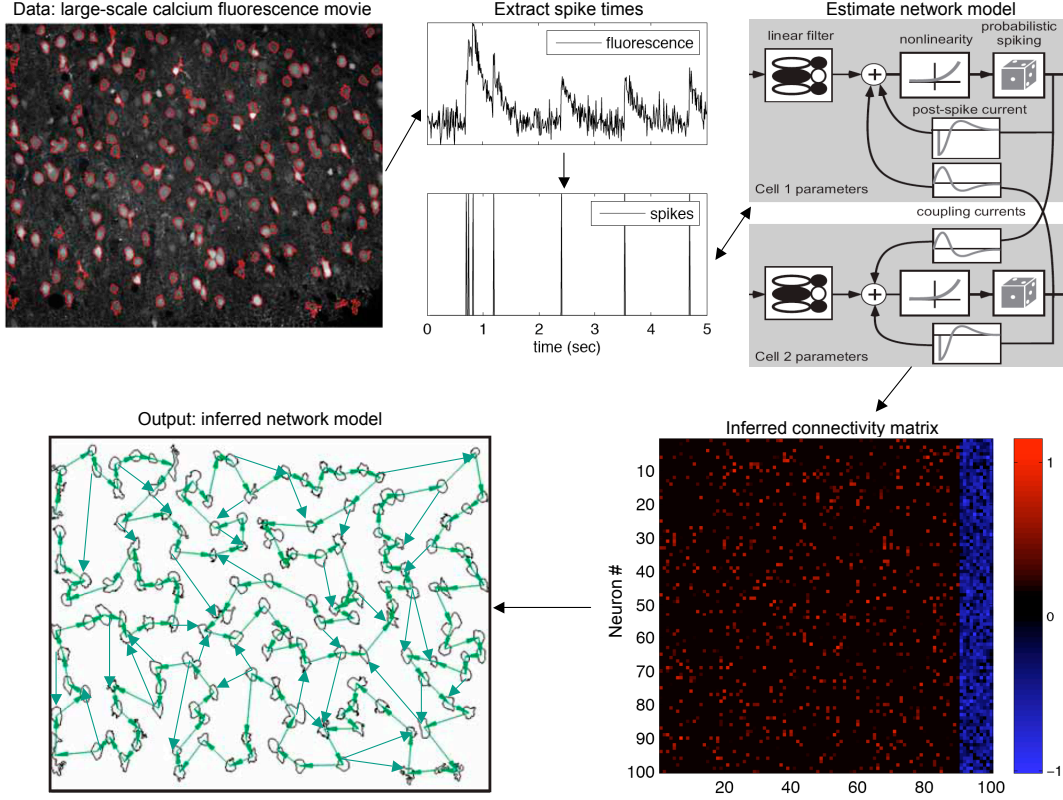


FIG 3. *Schematic overview. The raw observed data is a large-scale calcium fluorescence movie, which is pre-processed to correct for movement artifacts (in the in vivo setting) and find regions-of-interest (i.e., putative neurons); note that we have omitted details of these important preprocessing steps in this paper. Given the fluorescence traces from each neuron, we estimate the underlying spike trains (i.e., in time series of neural activity) using statistical deconvolution methods. Then we estimate the parameters of a network model, given the observed data. Our major goal is to obtain an accurate estimate of the network connectivity matrix, which summarizes the information we are able to infer about the local neuronal microcircuit. This figure adapted from personal communications with R. Yuste, B. Watson, and A. Packer.*

computer simulation. Each neuron also had an exponential refractory current (Koch, 1999).

Note that EPSP peak amplitudes cannot be used directly in Eq. (1), as a synaptic weight in our model — w_{ij} in Eq. (1) — is a dimensionless quantity representing the change in the spiking probability of neuron i given neuron j fired; whereas EPSP peak amplitude describes physiologically measured change in the membrane voltage of a neuron due to synaptic currents triggered by spike in neuron j . We must therefore find a way to relate the two.

Consider the above model for spiking, Eqs. (1) – (3). Let δP be the difference between the probability of neuron i spiking given that neuron j spiked in the previous time bin, $P[n_i(t) = 1 | n_j(t - \Delta) = 1]$, and the probability of neuron i spiking given that neuron j did

not spike in the previous time bin, $P[n_i(t)|n_j(t - \Delta) = 0]$:

$$\begin{aligned} \delta P &= P[n_i(t) = 1|n_j(t - \Delta) = 1] - P[n_i(t) = 1|n_j(t - \Delta) = 0] \\ (15) \quad &= \exp[-e^{b_i + w_{ij}\tau_w}\Delta] - \exp[-e^{b_i}\Delta] \end{aligned}$$

where τ_w accounts for the decay time constant of the spike history term. Now consider a simple, stochastic, integrate-and-fire neuron, with baseline voltage zero, spiking threshold one, EPSP amplitude V_E , and variance σ_v^2 :

$$\begin{aligned} V_i(t) &= V_i(t - \Delta) + V_E\delta(n_j(t - \Delta)) + \sigma_v\sqrt{\Delta}\varepsilon_i(t), & \text{if } V_i(t) < 1 \\ (16) \quad V_i(t) &= 0 & \text{if } V_i(t) \geq 1 \end{aligned}$$

In such a model, we again write δP :

$$\begin{aligned} \delta P &= \int_1^\infty \mathcal{N}(V_i(t - \Delta), \sigma^2) dV_i(t - \Delta) - \int_1^\infty \mathcal{N}(V_i(t - \Delta) + V_E, \sigma^2) dV_i(t - \Delta) \\ (17) \quad &= g(V_E) \end{aligned}$$

A little algebra yields:

$$(18) \quad w_{ij} = \frac{1}{\tau_w} \left(\ln \left[-\frac{1}{\Delta} \ln \left[g(V_E) + \exp(-e^{b_i}\Delta) \right] \right] - b_i \right)$$

which we used to obtain \mathbf{w} from the above mentioned parameters.

Parameters for the internal calcium dynamics and fluorescence observations were chosen according to our experience with several cells analyzed using algorithm of (Vogelstein et al., 2009), and conformed to previously published results (Yuste et al., 2006; Helmchen et al., 1996; Brenowitz and Regehr, 2007). Table 1 summarizes the details for each of the parameters in our model.

3. Results.

3.1. Inferring functional connectivity from simulated calcium imaging data. With neural population activity simulated as described in the previous section, we used our inference algorithms to reconstruct the functional connectivity matrix from simulated fluorescence data. Specifically, we estimated the connectivity matrix using both the embedded-chain-within-blockwise-Gibbs approach as well as factorized approximation. Figure 4 shows that factorized approximation was able to provide reconstructions almost as accurately as the exact embedded-chain-within-blockwise-Gibbs approach, $r^2 = 0.47$ versus $r^2 = 0.48$, when parameters corresponded to a realistic experiment, given 10 minutes of simulation data, and a population of $N = 25$ neurons. We also estimated the weights using the true spike trains, $r^2 = 0.7$ (not shown), and the spike trains down-sampled to the frame rates of calcium imaging, $r^2 = 0.57$. Importantly, the quality of our estimates using the fluorescence traces alone (and no electrophysiological data) approached that using the true down-sampled spike trains.

3.2. Impact of coarse time discretization of calcium imaging data and scale factor of inferred connection weights. As suggested by Figure 4, upon inferring connection weights using down-sampled spike trains (or noisy versions thereof), a scale error is introduced. This is curious because our model was designed to be asymptotically unbiased (Paninski et al., 2004). Possible

causes of this scale error include (i) insufficient data, (ii) model misspecification (the simulated model did not conform exactly to our assumed model, due to the shape of PSPs; see Methods for details), or (iii) coarse time discretization. To investigate what extent of the scale error is caused by the coarse time discretization, we performed the following heuristic argument.

The sufficient statistic for estimating the weights to neuron i in our model is simply $E[X_i(t), \mathbf{X}(t - \Delta) | \mathbf{F}; \theta]$, which depends only on t and $t - \Delta$. If, however, spike trains are down-sampled, such that observations are made only several time-bins, this statistic is not available. More specifically, it becomes unclear whether certain presynaptic spikes occurred in t or $t - \Delta$. Thus, some fraction of spikes causally involved in postsynaptic firing will appear coincidental. The fraction of spike that appear coincidental, but are actually causal, corresponds to the expected scale error.

To formalize the above argument, consider the following significantly simplified case of two neurons coupled with a small weight w_{ij} , simulated with a time step size of Δ . The sufficient statistic for estimating w_{ij} is simply the expected value of a spike from neuron i at time t , given a spike from neuron j at $t - \Delta$:

$$(19) \quad \begin{aligned} SS &= E[n_i(t) | n_j(t - \Delta) = 1] = E\left[1 - \exp\left(-e^{b_i + w_{ij}h_{ij}(t)}\right)\right] \\ &\approx \exp(-b_i)\Delta + f'(b_i)\exp(-t/\tau_h) \approx \exp(-b_i)\Delta + f'(b_i)w_{ij}\tau_h, \end{aligned}$$

where $f'(b) = df/dXXX$, and $b_i \gg w_{ij}$. The above approximations follow due to XXX, and are required because the expected value is analytically intractable due to the $h_{ij}(t)$ term.

Now, if the spike trains were down-sampled by a factor d , we must further approximate the sufficient statistics. In particular, we would not know precisely in which time of d time-bins

TABLE 1

Table of simulation parameters. $\mathcal{E}(\lambda)$ indicates an exponential distribution with mean λ , and $\mathcal{N}_p(\mu, \sigma^2)$ indicates a normal distribution with mean μ and variance σ^2 , truncated at lower bound $p\mu$. Units (when applicable) are given with respect to mean values (i.e., units are squared for variance).

Total neurons	10-500	#
Excitatory neurons	80	%
Connections sparseness	10	%
Baseline firing rate	5	Hz
EPSP peak height	$\sim \mathcal{E}(0.5)$	μV
IPSP peak height	$\sim -\mathcal{E}(2.3)$	μV
EPSP rise time	1	msec
IPSP rise time	1	msec
EPSP decay time	$\sim \mathcal{N}_{0.5}(10, 2.5)$	msec
IPSP decay time	$\sim \mathcal{N}_{0.5}(20, 5)$	msec
refractory time	$\sim \mathcal{N}_{0.5}(10, 2.5)$	msec
Calcium std. σ_c	$\sim \mathcal{N}_{0.4}(28, 10)$	μM
Calcium jump after spike, A_c	$\sim \mathcal{N}_{0.4}(80, 20)$	μM
Calcium baseline, C_b	$\sim \mathcal{N}_{0.4}(24, 8)$	μM
Calcium decay time, τ_c	$\sim \mathcal{N}_{0.4}(200, 60)$	msec
Dissociation constant, K_d	200	μM
Mean photon budget, α	1-80	Kph
Baseline fluorescence, β	XXX	XXX
Signal-dependent noise, γ	XXX	XXX
Signal-independent noise, σ^F	XXX	XXX

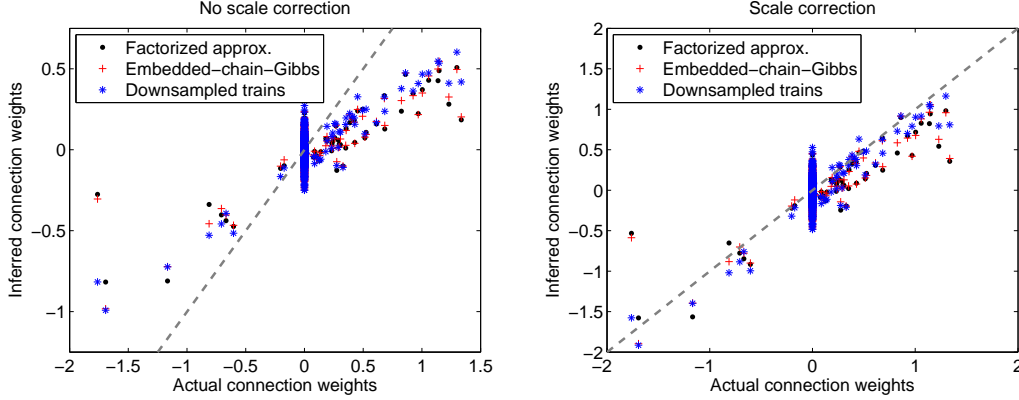


FIG 4. *Functional connectivity matrix can be reconstructed from calcium imaging data. Inferred connection weights are shown in a scatter plot versus real connection weights, with inference performed using factorized approximation, exact embedded-chain-within-blockwise-Gibbs approach, and spike trains down-sampled to the frame rate of the calcium imaging. A network of $N = 25$ neurons was used, firing at ≈ 5 Hz, and imaged for 10 min at intermediate SNR (photon budget 10 Kph/neuron/frame; see below). The factorized approximation had an $r^2 = 0.47$, as compared with the embedded-chain-within-blockwise-Gibbs method's $r^2 = 0.48$, and $r^2 = 0.57$ for down-sampled spike trains. The inferred connectivity show a clear scale error (left panel), which we correct using our theoretical scale correction factor (right panel; see Section 3.2 for details).*

the spike from neuron j occurred. Thus, the best we could do would be:

$$\begin{aligned}
 SS_d &= \sum_{k=1}^d E [n_i(t) | n_j(t - k\Delta) = 1, \{n_j(t - k'\Delta)\}_{k' \neq k} = 0] = \sum_{k=1}^d E [1 - \exp(-e^{b_i + w_{ij} \tilde{h}_{ij}^k(t)})] \\
 &\approx \exp(-b_i) d\Delta + f'(b) \int_0^\Delta \frac{dt'}{\Delta} \int_\Delta^{\Delta+\tau} dt w_{ij} \exp(-(t - t')/\tau^h) \\
 (20) \quad &\approx \exp(-b_i) d\Delta + f'(b) w_{ij} \frac{1 - \exp(-\Delta/\tau_h)}{\Delta/\tau_h^2},
 \end{aligned}$$

where $\tilde{h}_{ij}^k(t)$ is the expectation of $h_{ij}(t)$ given a spike from neuron j at k time-bins ago, the approximation follows using the same reasoning as above. The scale error that we expect to obtain from this coarse time discretization is thus:

$$(21) \quad \tilde{w}_{ij} \approx w_{ij} \times \text{scale factor} = w_{ij} \frac{SS}{SS_d} = w_{ij} \frac{1 - \exp(-\Delta/\tau_h)}{\Delta/\tau^h}.$$

This is the scale bias that we observe. In Figure 5 we plot the scale bias from Eq. 21 versus that empirically deduced from our simulations for different values of Δ . As can be seen in Figure 5, Eq. 21 describes observed scale bias very well.

An alternate way of dealing with this scale error would be to sub-sample spike trains, as discussed in (Vogelstein et al., 2009), to obtain spike train inferences at the desired temporal resolution. This possibility was not pursued here, as this approximation was sufficient for this work.

3.3. Impact of using priors on the inference. Taking into account simple prior information about the connectivity matrix results in dramatic improvement of the inferred connectivity

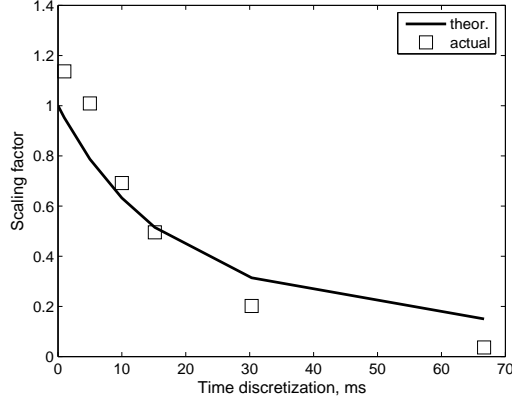


FIG 5. The low-frame rate of calcium imaging can explain the scale factor in inferred connectivity weights in Figure 4. Theoretically, scale factor may be evaluated by calculating what fraction of spikes from two neurons would occur within a single time-bin of width Δ (c.f. Eq. (21)). Plotted such theoretically calculated scale factor (line) vs. that observed empirically from our simulations (box), from a simulation of $N = 25$ neurons, $T = 10$ min. The error-bars correspond to 95% confidence intervals for scale factor estimate.

matrix using the same data. For example, imposing a sparse prior on a simulation of a network of $N = 50$ neurons imaged for $T = 10$ min, increased r^2 from $r^2 = 0.64$ to $r^2 = 0.85$ (Figure 6). Furthermore, the weights estimated using the sparse prior more reliably provide true connectivities, as well as the appropriate sign (i.e., excitatory or inhibitory) of each presynaptic neuron (Figure 7). Unfortunately, introducing a sparse prior further scales connectivity estimates, invalidating our analytic scale correction factor. Thus, a sparse prior can provide a more rapid estimate of relative connection strengths, but not absolute connection strengths, at this time.

Dale’s prior, on the other hand, only leads to $\approx 10\%$ change in r^2 of the reconstructed connectivity matrix for this simulation, and was not found significant. Further, imposing Dale’s prior when the sparse prior was initially enforced, typically resulted in no improvement to \mathbf{w} at all (not shown). As the sparse prior result achieved reconstruction accuracy close to the down-sampled spike train limit, there was limited room for improvement using Dale’s prior, and thus, it is not pursued further here.

3.4. Impact of experimental factors on estimator accuracy. What minimal conditions for the experimental setup should be met to for sufficient reconstruction accuracy of the connectivity from calcium imaging data? In Figures 8–10 we address this question. Figure 8 shows the quality of the inferred connectivity matrix as function of the imaging frame rate — imaging frame rates 30–60 Hz are needed to achieve meaningful reconstruction results. Frame rates ≈ 100 Hz allow achieving the same level of the connectivity matrix reconstruction that is possible with the exact knowledge of the true spike trains. Imaging frame 30–60 Hz are already in progress in existing experimental setups (Nguyen et al., 2001; Reddy and Saggau, 2005; Iyer et al., 2006; Salome et al., 2006; Reddy et al., 2008), each with the ability to significantly increase imaging rate, but costing a reduction in the number of observable neurons.

Figure 9 shows the quality of the inferred connectivity matrix as function of effective SNR

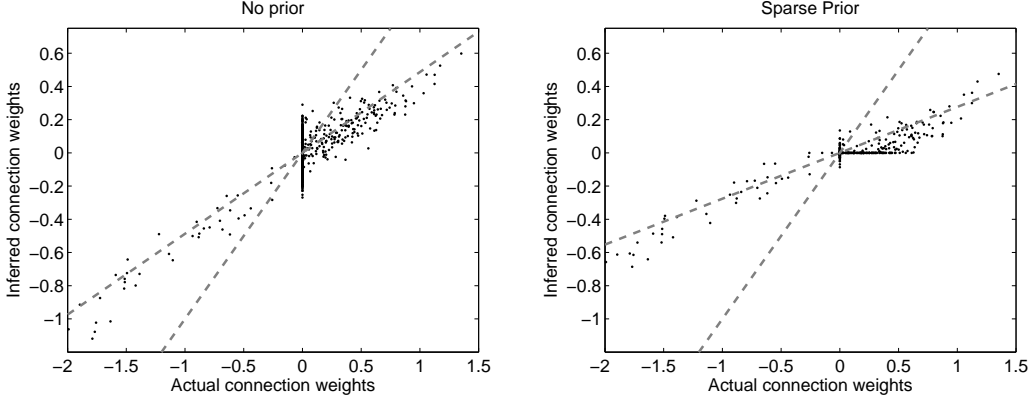


FIG 6. Connection weights reconstructed using no prior ($r^2 = 0.64$; left panel) and a sparse prior ($r^2 = 0.85$; right panel) are shown in a scatter plot for a network of $N = 50$ neurons, firing at ≈ 5 Hz, and imaged for $T = 10$ min. Clearly, the sparse prior reduces the relative error, as indicated by comparing the relative distance between the data points (black dots) to the best linear fit (black line), across the two panels.

and photon budget. Operationally, we define effective SNR as

$$(22) \quad \text{eSNR} = \frac{E[F_i(t) - F_i(t-1)|n_i(t) = 1]}{E[(F_i(t) - F_i(t-1))^2|n_i(t) = 0]^{1/2}},$$

and photon budget as γ^{-1} . Photon budget corresponds to the number of photons collected from single neuron within a single frame, at the peak of fluorescence intensity. XXX i don't see how this is true. XXX Note that the relationship between photon budget and eSNR depends on a number of other parameters, $\{\alpha, \beta, \sigma^F, K_d\}$, as well as the calcium concentration (which depends on spike rate, as well as $\{\tau^c, A, C^b\}$). From our experience with the analysis of real cells (Vogelstein et al., 2009), the eSNR for data collected at 15 Hz was ≈ 3 for in vitro data sets, and ≈ 9 for in vivo data sets (c.f. Figure 2). As can be seen from Figure 9, the effective SNR necessary for optimal reconstructions given a particular frame rate was ≈ 5 . This eSNR corresponded to photon budgets of ≈ 10 Kph/neuron/frame. Any lower, and reconstruction accuracy declined rapidly.

Finally, Figure 10 shows the quality of the inferred connectivity matrix as function of the experiment duration. The minimal amount of data for a particular r^2 depended substantially on whether the sparse prior was enforced. In particular, when not imposing a sparse prior, the calcium imaging duration necessary to achieve $r^2 = 0.5$ for the reconstructed connectivity matrix was $T \approx 10$ min, and $r^2 = 0.75$ was achieved at $T \approx 30$ min. With a sparse prior, $r^2 > 0.7$ was achieved already at $T \approx 5$ min. Furthermore, we observed that the accuracy of the reconstruction did not deteriorate with the size of the imaged neural population: the same reconstruction quality was observed with the same amount of data for $N = 50$ –200 neurons. This, at first unexpected result, is the direct consequence of the structure of the covariance matrix for \mathbf{w} , as will be discussed below. In all cases, good reconstructions were possible with only $T \sim 5$ –30 min of calcium imaging data.

3.5. Accuracy of the estimates and Fisher information matrix. Here we calculate theoretically the amount of spike trains data necessary to accurately estimate the functional connectivity matrix, \mathbf{w} . For clarity, we assume here that $\Delta \rightarrow 0$, and so $f(J) \approx e^J \Delta$, and that the spike trains are known perfectly, i.e. there is no corruption due to inference from

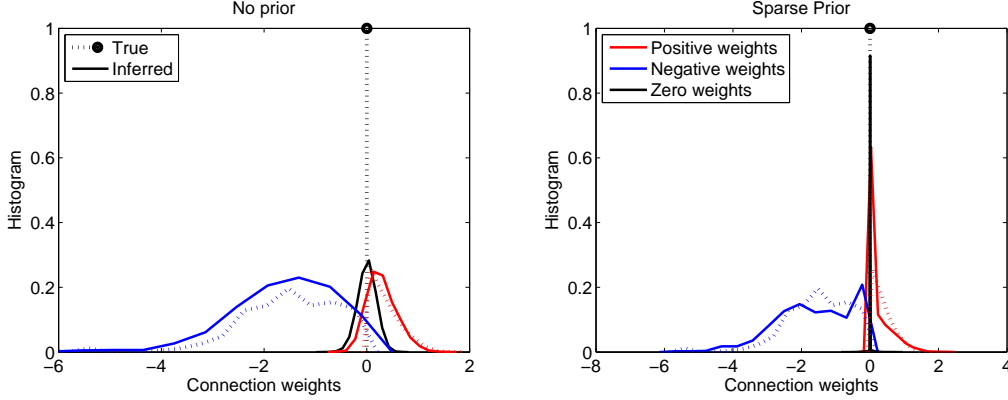


FIG 7. *Imposing a sparse prior on the distribution of connectivity weights, facilitates improving the inferred weights given the same amount of data. Shown here is the distribution of inferred connection weights using no prior (left panel) and a sparse prior (right panel) vs. true distributions. When the sparse prior is enforced, the appropriate number of connected pairs is identified (black lines), as well as the correct distribution of excitatory and inhibitory weights (red and blue lines, respectively). Distributions are shown for a network of $N = 200$ neurons, firing at ≈ 5 Hz, and imaged for $T = 10$ min.*

low-SNR calcium imaging data (an assumption validated by the above results). We also assume that the spikes only couple over a single time bin, so $h_{ij}(t) \equiv n_j(t - \Delta)$. Then, we can write the likelihood for the weights:

$$(23) \quad -\ln P[\mathbf{w}|\mathbf{X}] \propto -\ln P[\mathbf{X}|\mathbf{w}] = \sum_{i,t} [n_i(t) \ln f(J_i(t)) + (1 - n_i(t))(1 - f(J_i(t)))],$$

$$(24) \quad J_i(t) = b_i(t) + \sum_j w_{ij} h_{ij}(t) = b_i(t) + \sum_j w_{ij} n_j(t - \Delta).$$

The Fisher information matrix for $P[\mathbf{w}|\mathbf{X}]$ is therefore:

$$(25) \quad COV_{ij;i'j'}^{-1} = \left[\frac{\partial(-\ln P[\mathbf{w}|\mathbf{X}])}{\partial w_{ij} \partial w_{i'j'}} \right] = -\delta_{ii'} \sum_t \left[n_i(t) n_j(t - \Delta) n_{j'}(t - \Delta) \left(-\frac{f'(J_i(t))^2}{f(J_i(t))^2} + \frac{f''(J_i(t))}{f(J_i(t))} \right) - (1 - n_i(t)) n_j(t - \Delta) n_{j'}(t - \Delta) f''(J_i(t)) \right],$$

where f' and f'' correspond to the first and the second derivatives of our linking function (c.f Eq. (1)), and $\delta_{ii'}$ is the Kronecker's delta symbol, i.e., $\delta_{ii'} = 1$ for $i = i'$, and $\delta_{ii'} = 0$ otherwise. Letting $f(J) = e^J \Delta$, the first term in the sum in Eq. (25) cancels out, and the rest may be rewritten as:

$$(26) \quad \begin{aligned} COV_{ij;i'j'}^{-1} &= \delta_{ii'} T P[n_i(t) = 0, n_j(t - \Delta) = 1, n_{j'}(t - \Delta) = 1] \times E[e^{J_i(t)} | n_i(t) = 0, n_j(t - \Delta) = 1, n_{j'}(t - \Delta) = 1] \\ &= \delta_{ii'} T \left[(r\tau^h) \delta_{jj'} + O((r\tau^h)^2) \right] r. \end{aligned}$$

Here, $TP[n_i(t) = 0, n_j(t - \Delta) = 1, n_{j'}(t - \Delta) = 1]$ describes the number of nonzero terms in Eq. (25), corresponding to the condition that $(1 - n_i(t)) n_j(t - \Delta) n_{j'}(t - \Delta)$ is only nonzero when $n_i(t) = 0$, $n_j(t - \Delta) = 1$, and $n_{j'}(t - \Delta) = 1$. We let $r = E[e^{J_i(t)} | n_i(t) = 0, n_j(t - \Delta) = 1]$

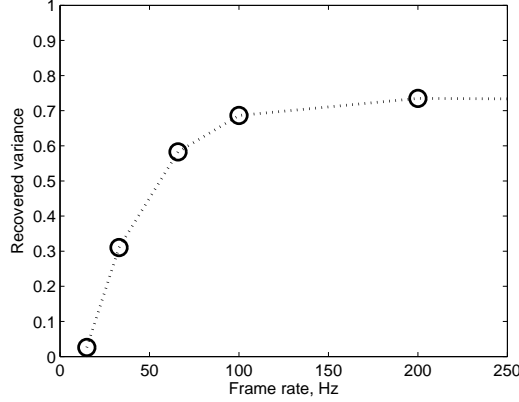


FIG 8. Accuracy of the inferred connectivity as function of the frame rate of calcium imaging. A network of $N = 25$ neurons, firing at ≈ 5 Hz and imaged for $T = 10$ min was simulated, and weights were inferred. At 100 Hz, r^2 using calcium imaging data reached the same level of accuracy as using the true spike trains from this simulation, indicating the further improvement could not be achieved by a further increase in frame rate.

$1, n_{j'}(t - \Delta) = 1]$ correspond to the average value of $f''(J_i(t))$, conditional on such nonzero events. $r\tau_h \ll 1$ is the probability for a neuron to spike over the time-interval τ_h .

The Fisher information matrix is block-diagonal, $COV_{ij;i'j'}^{-1} \propto \delta_{ii'}$, due to the structure of the log-likelihood $P[\mathbf{X}|\mathbf{w}]$ (it is a sum over i of independent terms), Eq. (23). From Eq. (26), we observe that Fisher information matrix is predominantly diagonal, because $COV_{ij;i'j'}^{-1} \propto \delta_{ii'}\delta_{jj'}$, and thus the covariance matrix, COV , can be computed trivially:

$$(27) \quad COV = (rT)^{-1}(r\tau^h I + O((r\tau_h)^2))^{-1} = (r^2\tau_h T)^{-1}I + O((r\tau_h)^2),$$

where I is the Identity matrix of appropriate size. For successful determination of the functional connectivity matrix \mathbf{w} , COV should be made smaller than the typical scale $\langle \mathbf{w}^2 \rangle$, so we require that:

$$(28) \quad T \approx (\langle \mathbf{w}^2 \rangle r^2 \tau^h)^{-1}.$$

For typical values of $\mathbf{w}^2 \approx 0.1$, $r \approx 5$ Hz and $\tau_h \approx 10$ msec, this estimate provides T of the order of hundreds of seconds. This theoretical estimate of the necessary amount of fluorescent data is in good agreement with our simulations.

Finally, because COV^{-1} is diagonal, this scale of COV does not depend on the number of neurons in the imaged neural population, N . Thus, the variance of the estimate \mathbf{w} does not degrade with the size of the imaged population, N , for the same amount of data, T .

3.6. Impact of strong correlations and deviations from generative model on the inference. “Anatomical” connectivity was recovered in our experiments despite potential problems noted in the literature, e.g. such as common input from correlated neurons (Nykamp, 2005; Nykamp, 2007), or unobserved neurons (Vidne et al., 2009). Estimation of the functional connectivity is fundamentally rooted in observing changes in the spike rate conditioned on the state of the other neurons. Intuitively, such estimation can be compared to observing changes in $f(\mathbf{n}(t)) \propto \exp(\sum_j w_{ij} n_j(t))$ for different neural configurations $\mathbf{n}(t)$, i.e. estimating a vector \mathbf{w}_i from a number of dot-products $\mathbf{w}_i \cdot \mathbf{n}(t)$. In order to properly estimate all components of

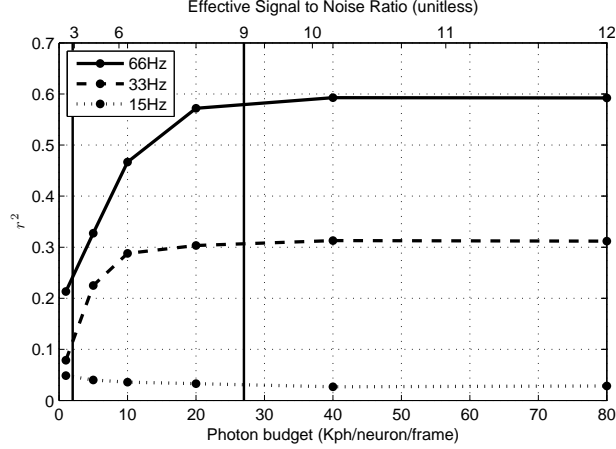


FIG 9. Accuracy of inferred connectivity as function of the noise amount in the calcium imaging data, as quantified by (i) eSNR and (ii) thousands of photons, per frame, per neuron (Kph/frame/neuron), for frame rates of 1, 5, 10, 15, 33, and 66 Hz. Photon counts on the order of 10–20 Kph/frame/neuron are required to achieve the upper bound determined by the frame rate. The connectivity matrix here was inferred from simulated fluorescence data using factorized approximation algorithm and the sparse prior. Simulation conditions are the same as in Figure 8. Vertical black lines correspond to the two example traces in Figure 2.

\mathbf{w}_i the set of available $\mathbf{n}(t)$ should be rich enough to span all N dimensions of \mathbf{w}_i . In case of independent firing such condition is clearly satisfied. Should this condition be violated, however, e.g. due to high correlation between spiking of few neurons, spike trains may not provide access to the true vector \mathbf{w}_i , and the connection weights inferred from such activity data may effectively “aggregate” true connection weights in arbitrary linear combinations.

We carried out a simulation of hypothetical “strongly” coupled neural network, where in addition to weak sparse connectivity we introduced sparse random strong connectivity component. In a sense, we allowed a fraction of neurons to couple strongly to the other neurons, thus, making them “command” neurons “driving” the activity of the rest of the population. The strength of strong connectivity component was chosen to dynamically build up the actual firing rate from the baseline rate of $r = \exp(b) \approx 1$ Hz to approximately 5 Hz. Such a network showed patterns of activity very different from the weakly coupled networks inspected above (Figure 11, top right). In particular, a large number of highly correlated events across many neurons were evident in this network. As expected, our algorithm was not able to identify the true connectivity matrix correctly in this scenario (Figure 11, bottom right panel). For ease of comparison, the left panels show a “typical” network (i.e., one lacking many strongly coupled neurons), and its associated connectivity inference. Note that the observability of the strongly coupled neurons does not save our inference.

On the other hand, our inference algorithm showed significant robustness to deviations of the actual data from our generative model. One important such deviation, which is likely to occur in the real experiments, is variation in the time scales of PSPs in different synapses. Up to now, all PSP time-scales were assumed to be the same in our inference algorithm as well as in the simulations, i.e., $\{\tau_{ij}^h\}_{i,j \leq N} = \tau_h$. In Figure 12 we introduce additional variability in τ_h from one neuron to another. Variability in τ_h results in added variance in the estimates of the connectivity weights w_{ij} through τ_h dependence of the scaling factor Eq. (21). Still, we found that such added variance was insignificant with τ_h varying for up to 25% from neuron

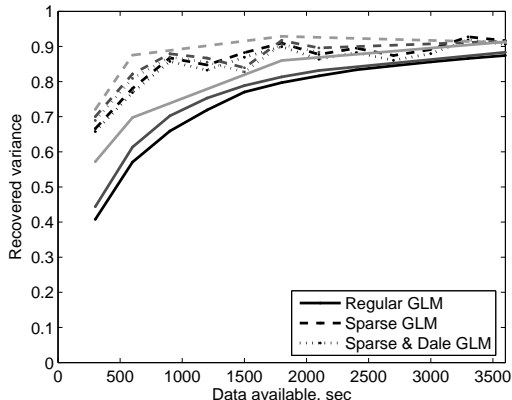


FIG 10. Accuracy of inferred connectivity as function of the imaging time and neural population size. Incorporating a sparse prior dramatically increases the reconstruction’s quality (dashed lines), over the no prior assumption (solid lines), given the same experimental duration. When the sparse prior is imposed, $T = 5$ min is already sufficient to recover 70% of the variance in the connection weights. Incorporating Dale’s prior leads to only marginal improvement (dotted line). Furthermore, reconstruction accuracy does not depend on the neural population size, N . Here, neural population from $N = 10$ to $N = 200$ were simulated for different T , $N = 100$ and 200 are shown (black and gray, respectively). Inhibitory weights for networks of different sizes were chosen to ensure mean firing rate ≈ 5 Hz, although actual firing rate varied somewhat.

to neuron.

4. Discussion. In this paper we develop a partial Bayesian approach for inferring functional connectivity in a population of spiking neurons observed using calcium imaging. While inferring functional connectivity from a set of simultaneous spike train recordings had been previously addressed for micro-electrode techniques (Paninski, 2003; ?), these approaches assumed observing the “true” spike trains of each observable neuron. However, evidence suggests that even state-of-the-art spike sorting algorithms only obtain approximately 90% accuracy in obtaining spike times (Harris et al., 2000; ?). With that in mind, (Rigat et al., 2006) developed an approach closely related to that here for such a scenario. In particular, they also consider a sparse prior, use a Bernoulli GLM model, and develop a Metropolis-within-Gibbs sampler to approximate the necessary sufficient statistics for their model. To our knowledge, we are the first address the problem of inferring connectivity from calcium population imaging data in a model based approach (though see (Roxin et al., 2008) for a related issue). Because calcium imaging, in principle, has capacity to image populations of cells containing $\approx 10^3$ – 10^6 neurons, this opens the way for analysis of micro-circuitry in large and complete populations of neurons in neocortex or other brain areas.

The main challenge in this problem is indirect nature of calcium imaging data, which provides only noisy, low-pass nonlinear filtered, temporally sub-sampled observations of spikes of individual neurons. In order to find connectivity parameters, in a fully Bayesian settings, the hidden spike trains need to be integrated out. Obtaining a joint sample of unobserved spike trains, needed to compute relevant integrals, is a very non-trivial problem given high dimensionality of the hidden state (which scales at least linearly with N). In particular, methods for analyzing calcium imaging data for single neurons, (Vogelstein et al., 2009), do not generalize well for this application. To solve this problem, in this paper we develop a new method for obtaining spike train samples from a population of coupled low-dimensional HMMs by embed-

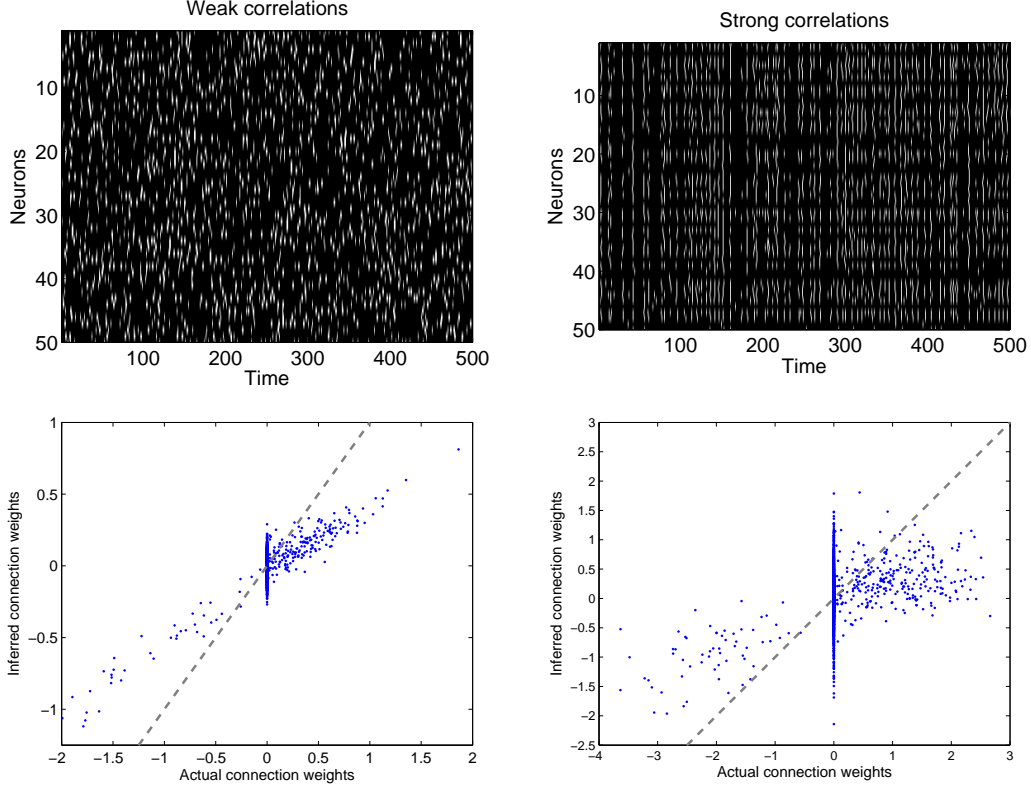


FIG 11. *Diverseness of observed neural activity patterns is required for functional connectivity to give access to the actual “anatomical” structure of the neural circuit. Here, 15 sec of simulated spike trains for a weakly coupled network (top left panel) and a network with strongly coupled component (top right panel) are shown. In weakly coupled networks, spikes are sufficiently uncorrelated to give access to enough different neural activity patterns to estimate the weights \mathbf{w} . In a strongly coupled case, many highly synchronous events are evident (top right panel), thus preventing observation of sufficiently rich ensemble of activity patterns. Accordingly, the connectivity estimates for the strongly coupled neural network (bottom right panel) does not represent the true connectivity of the circuit, even for the weakly coupled component. This is contrary to the weakly-coupled network (bottom left panel) where true connectivity is successfully obtained. Networks of $N = 50$ neurons firing at ≈ 5 Hz and imaged for $T = 10$ min were used to produce this figure.*

ding sampling chains of states from individual low-dimensional HMM within a Gibbs sampler that loops in a predefined order over different coupled HMMs. The functional connectivity matrix is then inferred by maximizing the expected value of posterior log-likelihood in EM framework. An exponential prior is used to enforce the sparseness condition of the objective connectivity matrix, which significantly reduces the minimal amount of data required for a particular reconstruction accuracy.

By applying this method to observations of spontaneous activity in a simulated population of neurons, we can efficiently infer the functional connectivity matrix from only ≈ 10 min of simulated calcium imaging data (c.f Figure 9, 10). While the embedded-chain-within-Gibbs methods leads to an exact locally MAP estimate, under reasonable calcium imaging conditions we find that significant simplification is possible, where the posterior distribution may be assumed to approximately factorize, $P(\mathbf{X}|\mathbf{F};\theta) \approx \prod P(X_i|F_i;\hat{\theta}_i)$. This allows one to obtain samples of joint spike trains much more easily, and in parallel. Since the maximization procedure in EM also can be straightforwardly parallelized, thanks to special structure of

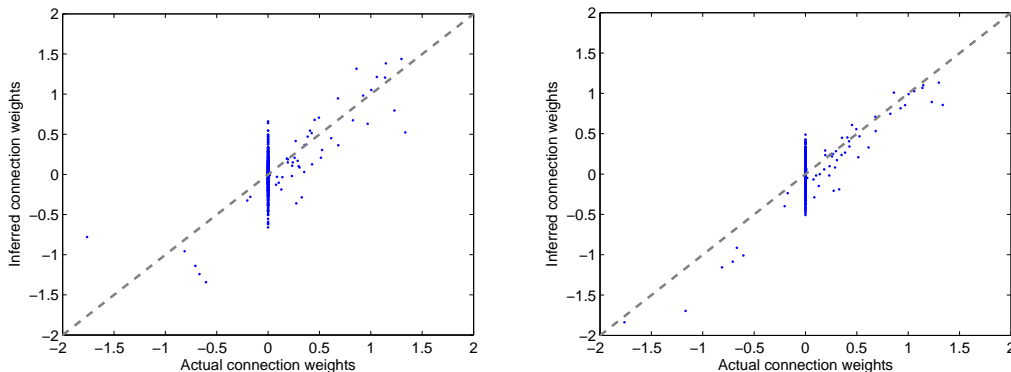


FIG 12. *Inference is robust to deviations of the data from our generative model. One such deviation, that should be expected in real data, is variability in the PSP time courses from neuron to neuron, and possibly synapse to synapse. With up to 25% variability allowed in PSP time scales τ_h (right panel), our algorithm provided reconstructions of almost the same quality as when all τ_h 's were the same (left panel). Simulation conditions were the same as in Figure 8.*

the posterior likelihood, the entire inference method can be easily implemented as a highly parallelized application, offering significant savings in data-processing time. If calculations are performed on a large high-performance cluster, reconstruction of the connectivity matrix from ≈ 10 min of calcium imaging data can be performed nearly in real time, by solving each neuron on a separate node and utilizing only about 10 minutes of computational time per each node. This is an important virtue of our method.

The above described approach differs significantly from naively computing pairwise measures, such as correlation coefficients, which are far faster to compute. In particular, our inferred weights depend on *all* the observed neurons, not simply the pairwise measures. In other words, the sufficient statistic for \mathbf{w}_i is $P[X_i(t), \mathbf{X}(t - \Delta) | \mathbf{F}]$, as compared with correlation-like measures that depend only on $P[X_i(t) | X_j(t - \Delta)]$. So, while a naive application of correlation coefficients might be attractive here, the resulting estimated “weights” are effectively useless (not shown).

A number of possible improvements of our method can be proposed. One of the biggest challenges for inferring neural connectivity from functional data is the presence of so called hidden inputs from unobserved neurons (Vidne et al., 2009). Since it is typically impossible to expect that activity of all neurons in a closed neural circuit can be monitored, such hidden inputs should be always anticipated in real imaging data. Correlations in hidden inputs are capable of successfully mimicking functional connections among different observed neurons, thus presenting a substantial challenge for estimating neural circuit’s connectivity from activity observations alone. Developing methods to cope with such hidden inputs is currently area of active research (Vidne et al., 2009).

Along with investigation of ways to combat the effect of unobserved neurons, we have considered several other potential directions for future improvements of our method. Incorporating photo-stimulation to activate or deactivate individual neurons or sub-populations may be used to significantly increase statistical power of a given set of observations (Boyden et al., 2005; Szobota et al., 2007). Although naturally observed activity may not allow reliable determination of circuit’s connectivity matrix, by utilizing external stimulation, a sufficiently rich sample of activity patterns may be collected, and true anatomical structure of the neu-

ral circuit may be inferred. Developing the optimal sequences of artificial stimuli and their implementation in the actual experiments are other important directions for future work.

Furthermore, improvements of the algorithms for faster implementation of both the E and M step of our algorithm are under development. Specifically, fast, non-negative deconvolution of calcium to infer spike trains is a promising alternative (Vogelstein et al., 2008). This fast algorithm utilizes the tridiagonal structure of the state-space problem, a interior-point approach to impose the non-negativity constraint, and Gaussian elimination to ascend the concave likelihood surface in $O(T)$ (Paninski et al., 2009). This approach only yields the MAP estimate of the most likely spike train, and so a true maximization step (integrating over a distribution) is not feasible. However, approximating the posterior with the MAP seems sufficient when SNR is sufficiently high (Vogelstein et al., 2008).

Several improvements in the model are also under investigation. Explicitly modeling Poisson statistics of the spike counts in time-bins with large width, Δ , rather than Bernoulli distribution used in this work, might helpful for fast spiking neurons. Modifications of our generative model allowing to deal with fluorescent signal non-stationarities, e.g. due to dye bleaching and drift, will be important to reliably apply our method to real data.

Finally, a fully Bayesian algorithm for estimating the posterior distributions of all the parameters, as opposed to only finding the MAP estimate, is of great interest. Such fully-Bayesian extension is conceptually simple: we just need to extend this work’s Gibbs sampler to additionally sample from θ given the spike trains \mathbf{X} . Since we already have a method for drawing the spike trains \mathbf{X} given θ and \mathbf{F} , with such an additional sampler we may obtain samples from $P(\mathbf{X}, \theta | \mathbf{F})$ simply by sampling from $\mathbf{X} \sim P(\mathbf{X} | \theta, \mathbf{F})$ and $\theta \sim P(\theta | \mathbf{X})$ within a Gibbs sampling procedure. Sampling from the posteriors $P(\theta | \mathbf{X})$ in the GLM setting is tractable using hybrid Monte Carlo methods, since all the posteriors are log-concave (Ishwaran, 1999; Gamerman, 1997; Gamerman, 1998; Ahmadian et al., 2009). All these advances are currently being pursued.

Acknowledgements. The authors would like to acknowledge Rafael Yuste, Brendon O. Watson, Adam Packer, Tanya Sippy, Tom Mrsic-Flogel and Vincent Bonin for data and helpful discussions.

References.

- Abeles, M. (1991). *Corticonics*. Cambridge University Press.
- Ahmadian, Y., Pillow, J., and Paninski, L. (2009). Efficient Markov Chain Monte Carlo methods for decoding population spike trains. *Under review, Neural Computation*.
- Andrieu, C., Doucet, A., and Holenstein, A. (2007). Particle markov chain monte carlo. *Working paper*.
- Bickel, P., Li, B., and Bengtsson, T. (2008). Sharp failure rates for the bootstrap particle filter in high dimensions. In Clarke, B. and Ghosal, S., editors, *Pushing the Limits of Contemporary Statistics: Contributions in Honor of Jayanta K. Ghosh*, pages 318–329. IMS.
- Binzegger, T., Douglas, R. J., and Martin, K. A. C. (2004). A Quantitative Map of the Circuit of Cat Primary Visual Cortex. *J. Neurosci.*, 24(39):8441–8453.
- Boyd, S. and Vandenberghe, L. (2004). *Convex Optimization*. Oxford University Press.
- Boyden, E. S., Zhang, F., Bamberg, E., Nagel, G., and Deisseroth, K. (2005). Millisecond-timescale, genetically targeted optical control of neural activity. *Nat Neurosci*, 8(9):1263–1268.

- Braitenberg, V. and Schuz, A. (1998). *Cortex: statistics and geometry of neuronal connectivity*. Springer, Berlin.
- Brenowitz, S. D. and Regehr, W. G. (2007). Reliability and heterogeneity of calcium signaling at single presynaptic boutons of cerebellar granule cells. *J Neurosci*, 27(30):7888–7898.
- Briggman, K. L. and Denk, W. (2006). Towards neural circuit reconstruction with volume electron microscopy techniques. *Current Opinions in Neurobiology*, 16:562.
- Brillinger, D. (1988). Maximum likelihood analysis of spike trains of interacting nerve cells. *Biological Cybernetics*, 59:189–200.
- Brillinger, D. (1992). Nerve cell spike train data analysis: a progression of technique. *Journal of the American Statistical Association*, 87:260–271.
- Buhl, E., Halasy, K., and Somogyi, P. (1994). Diverse sources of hippocampal unitary inhibitory postynaptic potentials and the number of synaptic release sites. *Nature*, 368:823–828.
- Candes, E. J. and Romberg, J. (2005). Practical signal recovery from random projections.
- Chornoboy, E., Schramm, L., and Karr, A. (1988). Maximum likelihood identification of neural point process systems. *Biological Cybernetics*, 59:265–275.
- Dempster, A., Laird, N., and Rubin, D. (1977). Maximum likelihood from incomplete data via the EM algorithm. *Journal Royal Stat. Soc., Series B*, 39:1–38.
- Djurisic, M., Antic, S., Chen, W. R., and Zecevic, D. (2004). Voltage imaging from dendrites of mitral cells: EPSP attenuation and spike trigger zones. *J. Neurosci.*, 24(30):6703–6714.
- Donoho, D. and Elad, M. (2003). Optimally sparse representation in general (nonorthogonal) dictionaries via L^1 minimization. *PNAS*, 100:2197–2202.
- Doucet, A., de Freitas, N., and N., G. (2001). *Sequential Monte Carlo in Practice*. Springer.
- Doucet, A., Godsill, S., and Andrieu, C. (2000). On sequential Monte Carlo sampling methods for Bayesian filtering. *Statistics and Computing*, 10:197–208.
- Escola, S. and Paninski, L. (2008). Hidden Markov models applied toward the inference of neural states and the improved estimation of linear receptive fields. *Under review, Neural Computation*.
- Feldmeyer, D., Egger, V., Lubke, J., and Sakmann, B. (1999). Reliable synaptic connections between pairs of excitatory layer 4 neurones within a single “barrel” of developing rat somatosensory cortex. *J Physiol*, 521 Pt 1:169–90.
- Feldmeyer, D. and Sakmann, B. (2000). Synaptic efficacy and reliability of excitatory connections between the principal neurones of the input (layer 4) and output layer (layer 5) of the neocortex. *J Physiol*, 525:31–9.
- Gamerman, D. (1997). Sampling from the posterior distribution in generalized linear mixed models. *Statistics and Computing*, 7(1):57–68.
- Gamerman, D. (1998). Markov chain monte carlo for dynamic generalised linear models. *Biometrika*, 85(1):215–227.
- Godsill, S., Doucet, A., and West, M. (2004). Monte Carlo smoothing for non-linear time series. *Journal of the American Statistical Association*, 99:156–168.
- Gomez-Urquijo, S. M., Reblet, C., Bueno-Lopez, J. L., and Gutierrez-Ibarluzea, I. (2000). Gabaergic neurons in the rabbit visual cortex: percentage, distribution and cortical projections. *Brain Res*, 862:171–9.
- Greenberg, D. S., Houweling, A. R., and Kerr, J. N. D. (2008). Population imaging of ongoing neuronal activity in the visual cortex of awake rats. *Nat Neurosci*.
- Gupta, A., Wang, Y., and Markram, H. (2000). Organizing principles for a diversity of gabaergic interneurons and synapses in the neocortex. *Science*, 287:273–8.

- Harris, K., Csicsvari, J., Hirase, H., Dragoi, G., and Buzsaki, G. (2003). Organization of cell assemblies in the hippocampus. *Nature*, 424:552–556.
- Harris, K. D., Henze, D. A., Csicsvari, J., Hirase, H., and Buzsaki, G. (2000). Accuracy of tetrode spike separation as determined by simultaneous intracellular and extracellular measurements. *Journal of Neurophysiology*, 81(1):401–414.
- Hatsopoulos, N., Ojakangas, C., Paninski, L., and Donoghue, J. (1998). Information about movement direction obtained by synchronous activity of motor cortical neurons. *PNAS*, 95:15706–15711.
- Helmchen, F., Imoto, K., and Sakmann, B. (1996). Ca^{2+} buffering and action potential-evoked Ca^{2+} signaling in dendrites of pyramidal neurons. *Biophys J*, 70(2):1069–1081.
- Ishwaran, H. (1999). Applications of hybrid Monte Carlo to Bayesian generalized linear models: quasicomplete separation and neural networks. *Journal of Computational and Graphical Statistics*, 8:779–799.
- Iyer, V., Hoogland, T. M., and Saggau, P. (2006). Fast functional imaging of single neurons using random-access multiphoton (RAMP) microscopy. *J Neurophysiol*, 95(1):535–545.
- Koch, C. (1999). *Biophysics of Computation*. Oxford University Press.
- Kulkarni, J. and Paninski, L. (2007). Common-input models for multiple neural spike-train data. *Network: Computation in Neural Systems*, 18:375–407.
- Lefort, S., Tómm, C., Floyd Sarria, J.-C., and Petersen, C. C. H. (2009). The excitatory neuronal network of the c2 barrel column in mouse primary somatosensory cortex. *Neuron*, 61:301–16.
- Li, K. and Duan, N. (1989). Regression analysis under link violation. *Annals of Statistics*, 17:1009–1052.
- Litke, A., Bezayiff, N., Chichilnisky, E., Cunningham, W., Dabrowski, W., Grillo, A., Grivich, M., Grybos, P., Hottowy, P., Kachiguine, S., Kalmar, R., Mathieson, K., Petrusca, D., Rahman, M., and Sher, A. (2004). What does the eye tell the brain? development of a system for the large scale recording of retinal output activity. *IEEE Trans Nucl Sci*, pages 1434–1440.
- Livet, J., Weissman, T., Kang, H., Draft, R., Lu, J., Bennis, R., Sanes, J., and Lichtman, J. (2007). Transgenic strategies for combinatorial expression of fluorescent proteins in the nervous system. *Nature*, 450:56–62.
- Luczak, A., Bartho, P., Marguet, S., Buzsaki, G., and Harris, K. (2007). Sequential structure of neocortical spontaneous activity in vivo. *PNAS*, 104:347–352.
- McLachlan, G. and Krishnan, T. (1996). *The EM Algorithm and Extensions*. Wiley-Interscience.
- Micheva, K. and Smith, S. (2007). Array tomography: A new tool for imaging the molecular architecture and ultrastructure of neural circuits. *Neuron*, 55:25–36.
- Mishchenko, Y. (2009). Strategies for identifying exact structure of neural circuits with broad light microscopy connectivity probes. *Preprint*: <http://precedings.nature.com/documents/2669/version/2>.
- Mishchenko, Y., Spacek, J., Mendenhall, J., Chklovskii, D., and Harris, K. M. (2009). Reconstruction of hippocampal ca1 neuropil at nanometer resolution reveals disordered packing of processes and dependence of synaptic connectivity on local environment and dendritic caliber. *Preprint*: <http://precedings.nature.com/documents/2669/version/2>.
- Neal, R., Beal, M., and Roweis, S. (2003). Inferring state sequences for non-linear systems with embedded hidden Markov models. *NIPS*, 16.
- Ng, A. (2004). Feature selection, L_1 vs. L_2 regularization, and rotational invariance. *ICML*,

21.

- Nguyen, Q. T., Callamaras, N., Hsieh, C., and Parker, I. (2001). Construction of a two-photon microscope for video-rate Ca^{2+} imaging. *Cell Calcium*, 30(6):383–393.
- Nykamp, D. (2007). A mathematical framework for inferring connectivity in probabilistic neuronal networks. *Mathematical Biosciences*, 205:204–251.
- Nykamp, D. Q. (2005). Revealing pairwise coupling in linear-nonlinear networks. *SIAM J Applied Mathematics*, 65(6):2005–2032.
- Paninski, L. (2003). Convergence properties of some spike-triggered analysis techniques. *Network: Computation in Neural Systems*, 14:437–464.
- Paninski, L. (2004). Maximum likelihood estimation of cascade point-process neural encoding models. *Network: Computation in Neural Systems*, 15:243–262.
- Paninski, L., Ahmadian, Y., Ferreira, D., Koyama, S., Rahnema, K., Vidne, M., Vogelstein, J., and Wu, W. (2009). A new look at state-space models for neural data. *Submitted*.
- Paninski, L., Fellows, M., Shoham, S., Hatsopoulos, N., and Donoghue, J. (2004). Superlinear population encoding of dynamic hand trajectory in primary motor cortex. *J. Neurosci.*, 24:8551–8561.
- Petersen, C. C. and Sakmann, B. (2000). The excitatory neuronal network of rat layer 4 barrel cortex. *J Neurosci*, 20(20):7579–86.
- Petrusca, D., Grivich, M. I., Sher, A., Field, G. D., Gauthier, J. L., Greschner, M., Shlens, J., Chichilnisky, E. J., and Litke, A. M. (2007). Identification and characterization of a Y-like primate retinal ganglion cell type. *J. Neurosci.*, 27(41):11019–11027.
- Pillow, J., Shlens, J., Paninski, L., Sher, A., Litke, A., Chichilnisky, E., and Simoncelli, E. (2008). Spatiotemporal correlations and visual signaling in a complete neuronal population. *Nature*, 454:995–999.
- Plesser, H. and Gerstner, W. (2000). Noise in integrate-and-fire neurons: From stochastic input to escape rates. *Neural Computation*, 12:367–384.
- Rabiner, L. (1989). A tutorial on hidden Markov models and selected applications in speech recognition. *Proceedings of the IEEE*, 77:257–286.
- Ramon y Cajal, S. (1904). *La Textura del Sistema Nerviosa del Hombre y los Vertebrados*. Moya.
- Ramon y Cajal, S. (1923). *Recuerdos de mi vida: Historia de mi labor cientifica*. Alianza Editorial.
- Reddy, G., Kelleher, K., Fink, R., and Saggau, P. (2008). Three-dimensional random access multiphoton microscopy for functional imaging of neuronal activity. *Nature Neuroscience*, 11(6):713–720.
- Reddy, G. D. and Saggau, P. (2005). Fast three-dimensional laser scanning scheme using acousto-optic deflectors. *J Biomed Opt*, 10(6):064038.
- Reyes, A., Lujan, R., Rozov, A., Burnashev, N., Somogyi, P., and Sakmann, B. (1998). Target-cell-specific facilitation and depression in neocortical circuits. *Nat Neurosci*, 1:279–285.
- Rigat, F., de Gunst, M., and van Pelt, J. (2006). Bayesian modelling and analysis of spatio-temporal neuronal networks. *Bayesian Analysis*, 1:733–764.
- Robert, C. and Casella, G. (2005). *Monte Carlo Statistical Methods*. Springer.
- Roxin, A., Hakim, V., and Brunel, N. (2008). The statistics of repeating patterns of cortical activity can be reproduced by a model network of stochastic binary neurons. *J. Neurosci.*, 28(42):10734–10745.
- Salome, R., Kremer, Y., Dieudonne, S., Leger, J.-F., Krichevsky, O., Wyart, C., Chatenay, D., and Bourdieu, L. (2006). Ultrafast random-access scanning in two-photon microscopy

- using acousto-optic deflectors. *Journal of Neuroscience Methods*, 154(1-2):161–174.
- Santhanam, G., Ryu, S. I., Yu, B. M., Afshar, A., and Shenoy, K. V. (2006). A high-performance brain-computer interface. *Nature*, 442:195–198.
- Sayer, R. J., Friedlander, M. J., and Redman, S. J. (1990). The time course and amplitude of epsps evoked at synapses between pairs of ca3/ca1 neurons in the hippocampal slice. *J. Neurosci.*, 10:826–36.
- Segev, R., Goodhouse, J., Puchalla, J., and Berry, M. (2004). Recording spikes from a large fraction of the ganglion cells in a retinal patch. *Nature Neuroscience*, 7:1154–1161.
- Shumway, R. and Stoffer, D. (2006). *Time Series Analysis and Its Applications*. Springer, 2nd edition.
- Song, S., Sjöström, P. J., Reigl, M., Nelson, S., and Chklovskii, D. B. (2005). Highly nonrandom features of synaptic connectivity in local cortical circuits. *PLoS Biology*, 3:e68.
- Stein, R. B., Weber, D. J., Aoyagi, Y., Prochazka, A., Wagenaar, J. B. M., Shoham, S., and Normann, R. A. (2004). Coding of position by simultaneously recorded sensory neurones in the cat dorsal root ganglion. *J Physiol (Lond)*, 560(3):883–896.
- Stevenson, I., Rebesco, J., Hatsopoulos, N., Haga, Z., Miller, L., and Koerding, K. (2008). Inferring network structure from spikes. *Statistical Analysis of Neural Data meeting*.
- Stevenson, I. H., Rebesco, J. M., Hatsopoulos, N. G., Haga, Z., Miller, L. E., and Kording, K. P. (2009). Bayesian inference of functional connectivity and network structure from spikes. *IEEE Trans. Neural Systems and Rehab.*, 17:203–13.
- Stosiek, C., Garaschuk, O., Holthoff, K., and Konnerth, A. (2003). In vivo two-photon calcium imaging of neuronal networks. *Proceedings of The National Academy Of Sciences Of The United States Of America*, 100(12):7319–7324.
- Szobota, S., Gorostiza, P., Del Bene, F., Wyart, C., Fortin, D. L., Kolstad, K. D., Tulyathan, O., Volgraf, M., Numano, R., Aaron, H. L., Scott, E. K., Kramer, R. H., Flannery, J., Baier, H., Trauner, D., and Isacoff, E. Y. (2007). Remote control of neuronal activity with a light-gated glutamate receptor. *Neuron*, 54:535–545.
- Thompson, A., Girdlestone, D., and West, D. (1988). Voltage-dependent currents prolong single-axon postsynaptic potentials in layer III pyramidal neurons in rat neocortical slices. *J Neurophysiol*, 60:1896–1907.
- Tibshirani, R. (1996). Regression shrinkage and selection via the lasso. *Journal of the Royal Statistical Society. Series B*, 58:267–288.
- Tipping, M. (2001). Sparse Bayesian learning and the relevance vector machine. *Journal of Machine Learning Research*, 1:211–244.
- Truccolo, W., Eden, U., Fellows, M., Donoghue, J., and Brown, E. (2005). A point process framework for relating neural spiking activity to spiking history, neural ensemble and extrinsic covariate effects. *Journal of Neurophysiology*, 93:1074–1089.
- Tsien, R. Y. (1989). Fluorescent probes of cell signaling. *Ann. Rev. Neurosci.*, 12:227–253.
- Vidne, M., Kulkarni, J., Ahmadian, Y., Pillow, J., Shlens, J., Chichilnisky, E., Simoncelli, E., and Paninski, L. (2009). Inferring functional connectivity in an ensemble of retinal ganglion cells sharing a common input. *COSYNE*.
- Vogelstein, J., Babadi, B., Watson, B., Yuste, R., and Paninski, L. (2008). Fast nonnegative deconvolution via tridiagonal interior-point methods, applied to calcium fluorescence data. *Statistical analysis of neural data (SAND) conference*.
- Vogelstein, J. T., Watson, B. O., Packer, A. M., Yuste, R., Jerny, B., and Paninski, L. (2009). Spike inference from calcium imaging using sequential monte carlo methods. *Preprint*.

- Wallace, D., zum Alten Borgloh, S., Astori, S., Yang, Y., Bausen, M., K
 ”ugler, S., Palmer, A., Tsien, R., Sprengel, R., Kerr, J., Denk, W., and Hasan, M. (2008).
 Single-spike detection in vitro and in vivo with a genetic Ca²⁺ sensor. *Nature methods*,
 5(9):797–804.
- Yaksi, E. and Friedrich, R. W. (2006). Reconstruction of firing rate changes across neuronal
 populations by temporally deconvolved Ca²⁺ imaging. *Nature Methods*, 3(5):377–383.
- Yasuda, R., Nimchinsky, E. A., Scheuss, V., Pologruto, T. A., Oertner, T. G., Sabatini, B. L.,
 and Svoboda, K. (2004). Imaging calcium concentration dynamics in small neuronal
 compartments. *Sci STKE*, 219:p15.
- Yuste, R., Konnerth, A., Masters, B., et al. (2006). *Imaging in Neuroscience and Development*,
A Laboratory Manual.

YURIY MISHCHENKO
 CITY STREET IN TURKEY
 E-MAIL: y@somewhere.com

JOSHUA VOGELSTEIN
 JOHNS HOPKINS UNIVERSITY
 3400 N. CHARLES ST.
 BALTIMORE, MD, 21205
 E-MAIL: joshuav@jhu.edu

LIAM PANINSKI
 ADDRESS
 USUALLY FEW LINES LONG
 E-MAIL: liam@stat.columbia.edu
 URL: <http://www.foo.com>